

## Article

# Genesis of the Beizhan Iron Deposit in Western Tianshan, China: Insights from Trace Element and Fe-O Isotope Compositions of Magnetite

Yan Li <sup>1,2</sup>, Zongsheng Jiang <sup>1,\*</sup>, Dachuan Wang <sup>3</sup>, Zuoheng Zhang <sup>4</sup> and Shigang Duan <sup>1</sup>

- <sup>1</sup> MNR Key Laboratory of Metallogeny and Mineral Assessment, Institute of Mineral Resources, Chinese Academy of Geological Sciences, Beijing 100037, China; 3009200001@email.cugb.edu.cn (Y.L.); duanshigang@mail.cgs.gov.cn (S.D.)
- <sup>2</sup> School of Gemmology, China University of Geosciences, Beijing 100083, China
- <sup>3</sup> Institut für Mineralogie, Leibniz Universität Hannover, 30167 Hannover, Germany; d.wang@mineralogie.uni-hannover.de
- <sup>4</sup> Institute of Geophysical and Geochemical Exploration, Chinese Academy of Geological Sciences, Langfang 065000, China; zhang.zuoheng@163.com
- \* Correspondence: jiangzongsheng@mail.cgs.gov.cn

**Abstract:** The Beizhan iron deposit (468 Mt at an average grade of 41% Fe) is the largest iron deposit in the Awulale iron metallogenic belt of Western Tianshan, northwest China. The high-grade magnetite ores are hosted in the Carboniferous volcanic rocks with extensive development of skarn alteration assemblages. While considerable progress has been made in understanding the characteristics of Beizhan and its genetic association with volcanic rocks, the genetic models for ore formation are poorly constrained and remain controversial. This study combines detailed petrographic investigations with in situ LA-ICP-MS analyses of trace elements and Fe-O isotope compositions of magnetite to elucidate the origin of magnetite and the conditions of ore formation. The trace element concentrations in magnetite unveil intricate origins for various ore types, implying the precipitation of magnetite from both magmatic and hydrothermal fluids. The application of the Mg-in magnetite thermometer ( $T_{\text{Mg-mag}}$ ) reveals a notable temperature divergence across different magnetite varieties, spanning from relatively higher temperatures in magmatic brecciated magnetite (averaging ~641 and 612 °C) to comparatively lower temperatures in hydrothermal platy magnetite (averaging ~552 °C). The iron isotopic composition in massive and brecciated magnetite grains, characterized by lighter  $\delta^{56}\text{Fe}$  values (ranging from  $-0.078$  to  $+0.005\text{‰}$  and  $-0.178$  to  $-0.015\text{‰}$ , respectively), suggest a magmatic or high-temperature hydrothermal origin. Conversely, the heavier  $\delta^{56}\text{Fe}$  values observed in platy magnetite ( $+0.177$  to  $+0.200\text{‰}$ ) are attributed to the influence of pyrrhotite, signifying late precipitation from low-temperature hydrothermal fluids. Additionally, the  $\delta^{18}\text{O}$  values of magnetite, ranging from  $+0.6$  to  $+4.6\text{‰}$ , provide additional evidence supporting a magmatic-hydrothermal origin for the Beizhan iron deposit. Overall, the identified genetic associations among the three magnetite types at Beizhan provide valuable insights into the evolution of ore-forming conditions and the genesis of the deposit. These findings strongly support the conclusion that the Beizhan iron deposit underwent a process of magmatic-hydrothermal mineralization.

**Keywords:** magnetite; trace elements; Fe-O isotopes; magmatic-hydrothermal process; Beizhan iron deposit; Western Tianshan



**Citation:** Li, Y.; Jiang, Z.; Wang, D.; Zhang, Z.; Duan, S. Genesis of the Beizhan Iron Deposit in Western Tianshan, China: Insights from Trace Element and Fe-O Isotope Compositions of Magnetite. *Minerals* **2024**, *14*, 304. <https://doi.org/10.3390/min14030304>

Academic Editor: Simon Paul Johnson

Received: 4 February 2024  
Revised: 25 February 2024  
Accepted: 28 February 2024  
Published: 14 March 2024



**Copyright:** © 2024 by the authors. Licensee MDPI, Basel, Switzerland. This article is an open access article distributed under the terms and conditions of the Creative Commons Attribution (CC BY) license (<https://creativecommons.org/licenses/by/4.0/>).

## 1. Introduction

The Awulale iron metallogenic belt (AIMB) in Western Tianshan, NW China, hosts several large-tonnage magnetite deposits that are closely associated with the coeval Carboniferous calc-alkaline volcanic and plutonic rocks (Figure 1) [1]. These deposits collectively have a total resource exceeding 1200 million metric tons (Mt) of Fe [2] with a significant

proportion of high-grade ores, providing attractive targets for the exploration and exploitation of iron in China. As a group, these deposits share many geological, mineralogical, and geochemical similarities with the volcanic-hosted iron oxide–apatite (IOA) deposits and magnetite-only deposits in, for example, the Chilean iron belt [3–8] and Southeast Missouri, USA [9–11]. Although the genetic link between volcanic processes and ore deposit formation seems to be unequivocal, the large variability of mineralogical characteristics found in these deposits has resulted in several disagreements regarding their origin and classification [12].

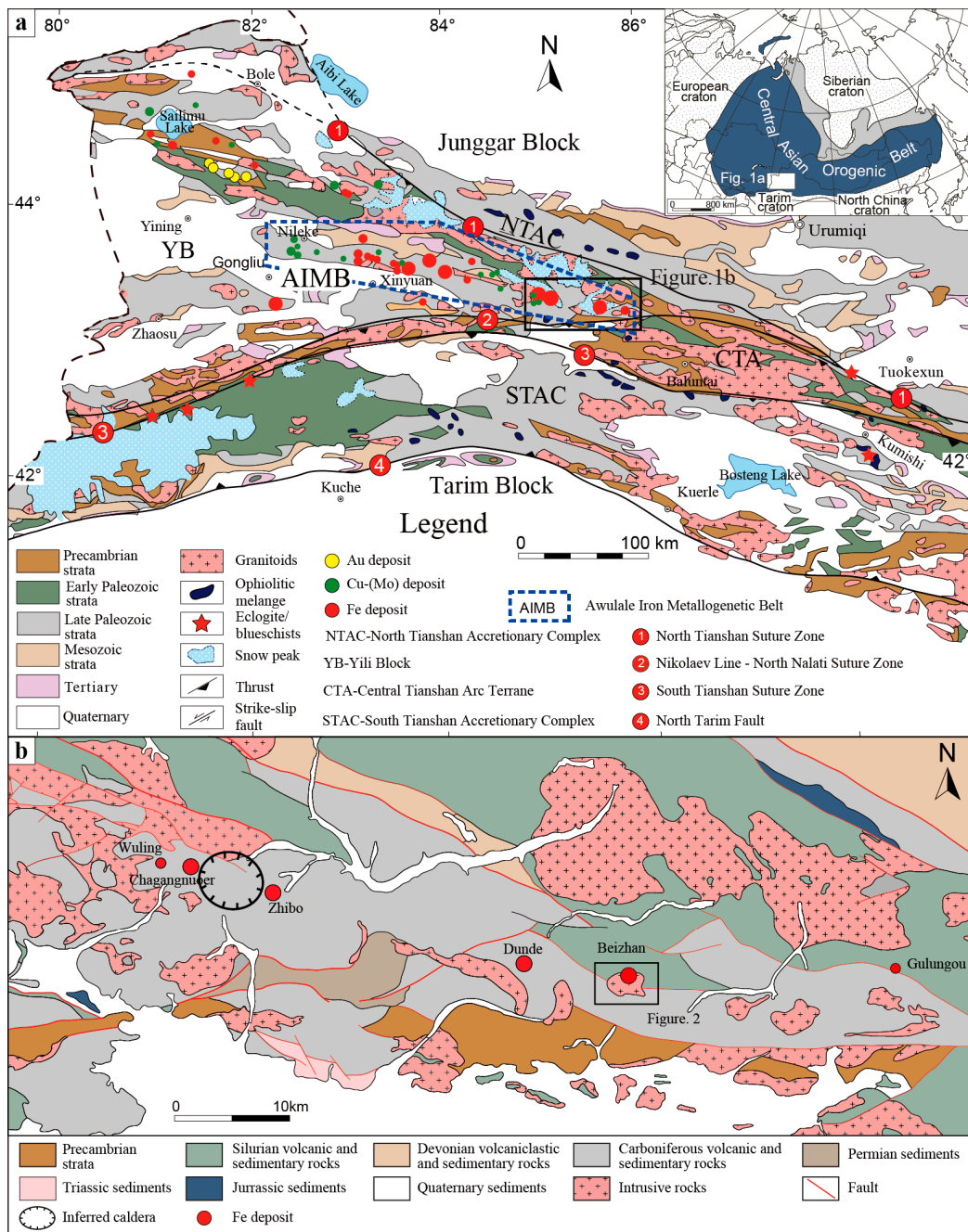


**Figure 1.** (a) Geological map of the Western Tianshan region in NW China showing the Awulale iron metallogenic belt and the major volcanic-hosted iron deposits (simplified from [13,14]). Inset map shows the location of Western Tianshan within the Central Asian Orogenic Belt (modified from [15]). (b) Geological map of the eastern part of the Awulale iron metallogenic belt showing the location of the Beizhan iron deposit (modified from [13]).

The Beizhan iron deposit, with a total resource of 468 Mt at 41% Fe [16], ranks among the largest iron deposits in the AIMB. It was previously considered to be a submarine volcanic-hosted iron deposit [2] or an iron skarn deposit [13,16,17]. Pan et al. [18] proposed that the iron ores in the carbonate rocks at Beizhan are sedimentary in origin and overprinted by later hydrothermal mineralization. More recently, Li et al. [19] identified co-existing IOA and iron skarn ores proximal to a dioritic–granitic intrusion and suggested that the IOA ores likely formed from high-temperature hydrothermal fluids from the dioritic intrusion, while the iron skarn ores originated from a relatively low-temperature and more evolved hydrothermal fluid. These varying interpretations highlight the complexity of the iron mineralization at Beizhan and emphasize the need for a better understanding of the ore-forming processes.

In this study, we investigated the chemistry of magnetite by using an electron probe micro analyzer (EPMA) and laser ablation inductively coupled mass spectroscopy (LA-ICP-MS) to classify compositional types of magnetite and unravel the genesis of iron mineralization at Beizhan. The formation temperatures of magnetite were obtained by applying the Mg-in magnetite thermometer ( $T_{\text{Mg-mag}}$ ) [20], which further gives key insights into the ore-forming processes. Furthermore, we use the Fe and O isotopes of magnetite to fingerprint the source of metals and ore fluids in the deposit.

## 2. Geological Background

### 2.1. Geologic Setting of Western Tianshan

Western Tianshan represents the western segment of the Tianshan orogenic belt, which forms part of the southwestern margin of the Central Asian Orogenic Belt (CAOB) [15]. It is subdivided, from north to south, into four tectonic terranes—the North Tianshan Accretionary Complex, the Yili Block, the Central Tianshan Arc Terrane, and the South Tianshan Accretionary Complex—each separated from the other by major suture zones and regional-scale strike–slip faults (Figure 1a) [21–24].

The Yili Block is underlain by a Precambrian basement, which comprises Proterozoic gneisses, schists, carbonates, and clastic rocks [14,21,24]. Granitic gneisses with U–Pb zircon ages of  $1609 \pm 40$  Ma [25] and  $919 \pm 6$  Ma [26] were reported in the northern margin of the Yili Block and represent the oldest magmatic events in Western Tianshan. These basement rocks are overlain by Mesoproterozoic to Phanerozoic marine sedimentary and volcanic sequences and intruded by numerous Neoproterozoic to Permian granitoids [14,24]. The closure of three Paleozoic oceans (the Terskey, South Tianshan, and North Tianshan oceans) during the Neoproterozoic to Paleozoic led to the amalgamation of the Yili Block with other terranes and the eventual formation of the Tianshan orogenic belt [24,27,28].

A large variety of mineral deposits are associated in space and time with the Late Paleozoic volcanic and subvolcanic rocks (Figure 1a), including porphyry Cu–(Mo) deposits, epithermal Au deposits [29], and volcanic-hosted iron oxide deposits [2,30].

### 2.2. Iron Mineralization in Western Tianshan

In the eastern section of Western Tianshan, a cluster of iron oxide deposits constitute an approximately 250 km long and 20 km wide iron belt, referred to as the Awulale iron metallogenic belt (Figure 1a). The AIMB has a collective resource of 1200 Mt [2] and represents one of the most substantial accumulations of high-grade iron ore in China [31].

These iron deposits primarily occur within the Carboniferous volcanic rocks of the Dahalajunshan Formation. Most iron deposits, such as Zhibo, Beizhan, and Chagangnuoer, are dominated by Ti-poor magnetite as the only economically extractable metal, except for the Dundee deposit, where significant zinc and gold mineralization occur around the magnetite ore bodies. Magnetite mineralization in these deposits was accompanied by extensive alteration, primarily involving Ca, Na, and K metasomatism, but differ in terms of alteration assemblages [32–36], possibly related to the differences in chemical composition of host rocks and ore-forming fluids. Several proposed genetic models for these deposits include skarn, volcanic–hydrothermal, hydrothermal replacement of volcanic rocks, and

exhalative–sedimentary in origin [13,16,37,38]. Based on in situ trace element and Fe isotope analysis of magnetite from the Zhibo and Changanuoer deposits, Günther et al. [12] proposed that most massive ores have an ortho-magmatic origin, while re-precipitated skarn-type iron ore is of hydrothermal origin.

The distribution of these deposits appears to be controlled by several volcano-hydrothermal centers in the region. Iron ore mineralization in lavas is typically observed in close proximity to the volcanic vent, while in pyroclastic–sedimentary rocks, it tends to occur at a more distal location [39]. Radiometric dates, including the Ar-Ar ages of muscovite, the Re-Os ages of pyrite, the Sm-Nd ages of garnet, and the U-Pb ages of titanite, demonstrate that iron mineralization mainly occurred around 330–300 Ma [33,36,40,41], overlapping ages for the host volcanic rocks [42–45]. The close spatial and temporal association, coupled with geological and geochemical evidence, strongly support a genetic link between the ore deposit and the host volcanic rocks [41].

### 3. Geology of the Beizhan Iron Deposit

The Beizhan iron deposit is situated on the northern limb of the Gongnaisi synclinorium, located in the eastern sector of the AIMB (Figure 1b) [32,40]. The deposit has undergone significant folding and faulting, resulting in complex crustal structures (Figure 2). Nine major compressional faults have been identified within the deposit. The presence of a volcano in the deposit is evidenced by effusive eruptions of andesitic lavas, explosive eruptions of tuff units, and the development of caldera structures, which are associated with the development of ring faults and dikes [46].

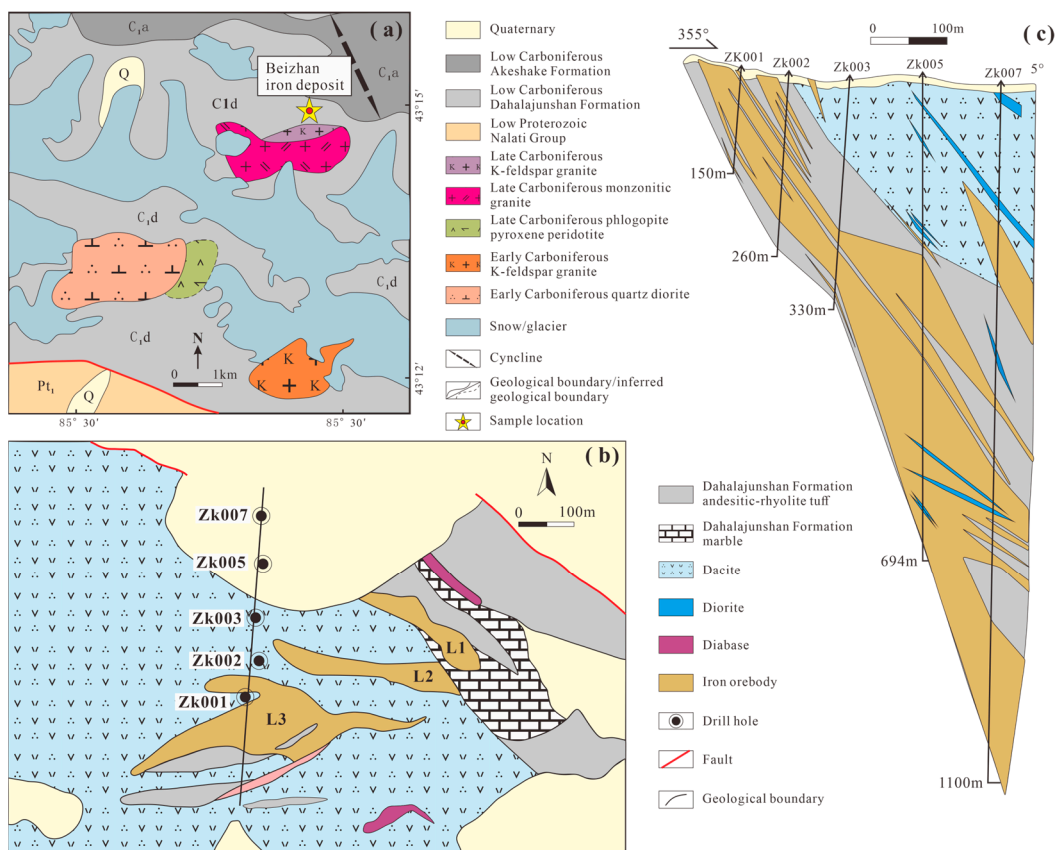


**Figure 2.** (a) Geological sketch map of the Beizhan iron deposit (modified from [47]). (b) Close-up geological map showing the main magnetite orebodies in the Beizhan iron deposit (modified from [16,48]). (c) Selected cross section of the Beizhan iron deposit (modified from [17,40]).

The Carboniferous Dahalajunshan Formation that hosts the deposit comprises basaltic andesite, andesite, dacite, rhyolite, limestone, basaltic tuff, and andesitic-rhyolitic tuff (Figure 2). Zircon U-Pb dating of the basaltic andesite and dacite has provided ages of  $320.6 \pm 2.2$  Ma and  $329.1 \pm 1.0$  Ma [49,50]. The volcanic rocks have been intruded by Late Carboniferous K-feldspar granite, diabase dike, and diorite. The geochemical and geological features of these igneous rocks suggest that the volcanic suites erupted in a continental arc setting, while the Late Carboniferous granites, diabase, and diorite dikes formed in an extensional setting [51].

The Beizhan deposit comprises six magnetite orebodies (L1–L6) that are generally concordant with the wall rocks. L3 is the dominant orebody and contains ~99% of the total ore resources of the deposit. The total iron content (TFe) of the ore body varies from 23% to 64.3%, with an average of 40.5%. The orebody is lensoid, veined, and stratiform, strikes northwest, and dips  $37^\circ$  to  $40^\circ$  to the north (Figure 2c). It extends over a strike length of about 880 m and a vertical extent of over 300 m, with a thickness up to 295 m in the deeper levels.

The magnetite mineralization dominantly occurs as massive, disseminated, brecciated, and vein ores (Figures 3 and 4). The massive ores represent the high-grade component of the mineralization and are composed predominantly of euhedral to subhedral granular magnetite with interspersed pyrite and silicate minerals (Figures 3a–c and 4a,b). Disseminated ores are widespread in the mineralization zones but commonly occur in proximity to massive ores or in the host rock surrounding the veins (Figure 3d,e). In disseminated ores, magnetite occurs as disseminated subhedral to anhedral grains intergrown with gangue minerals (Figure 4c). Platy magnetite is also present in disseminated ores in association with platy pyrrhotite (Figure 3f). The brecciated ores are defined by subangular fragments of volcanic rocks embedded in a magnetite matrix, with locally observed potassic and silicic alteration in the host rock fragments (Figure 3g,h and Figure 4d). Locally, magnetite occurs as veins and fracture fillings in altered country rocks (Figure 3i).

The gangue minerals are predominantly composed of calcite, ankerite, chlorite, serpentine, tourmaline, epidote, actinolite, and phlogopite with minor garnet, diopside, forsterite, titanite, and apatite. Pyrrhotite and pyrite are the most common sulfides, while chalcopyrite is typically present in trace amounts (Figure 4e,f).

The paragenetic sequence of the Beizhan iron deposit was subdivided into four stages based on field and petrographic observations (Figure 5). The skarn stage (I) is characterized by the development of skarn minerals, including garnet, diopside, and forsterite. The magnetite stage (II) represents the primary stage of magnetite mineralization, accompanied by minor precipitation of hematite, apatite, actinolite, and tremolite. The sulfide stage (III) is marked by veins of sulfide minerals such as pyrrhotite, pyrite, sphalerite, and chalcopyrite, often closely associated with magnetite ore. The chlorite-carbonate stage (IV) is represented by the formation of carbonate, chlorite, and serpentine, along with small quantities of magnetite and hematite.

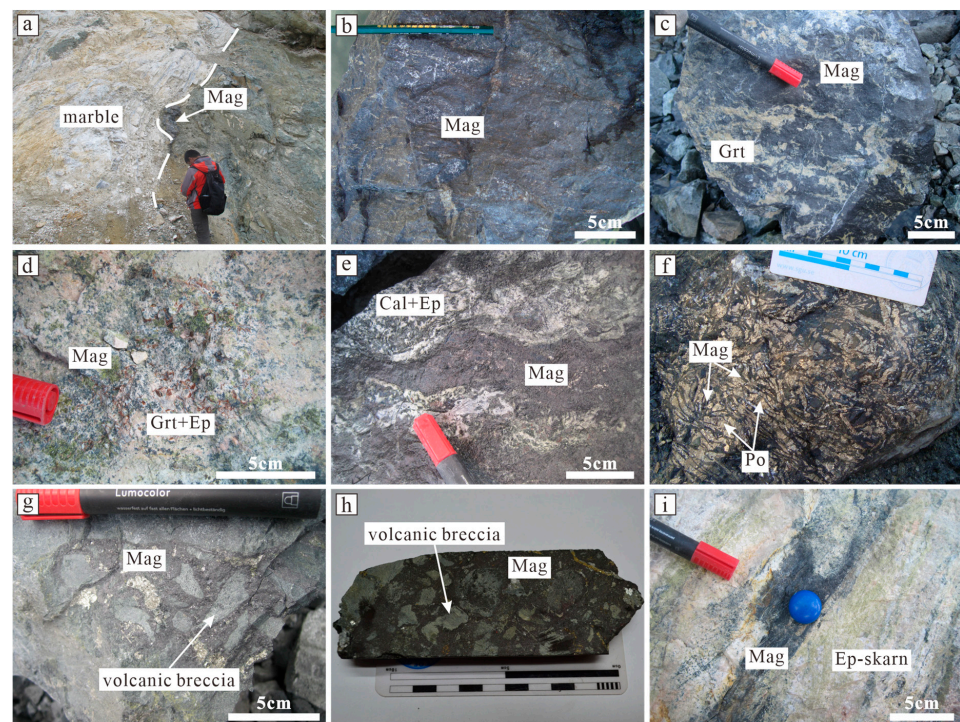


**Figure 3.** Photographs of the different ore types in the Beizhan iron deposit. (a) Massive magnetite (Mag) ores at the contact between altered host rock and marble. (b) Massive magnetite ore. (c) Massive magnetite ore with fracture infill of garnet (Grt) skarn. (d) Disseminated magnetite in garnet–epidote (Ep) skarn. (e) Disseminated magnetite in calcite (Cal)–epidote veins in proximity to massive ores. (f) Platy magnetite in association with platy pyrrhotite (Po). (g) Contact between host volcanic rock and magnetite ore, where volcanic breccias are cemented by magnetite. (h) Volcanic breccias in the magnetite matrix. (i) Veins of magnetite in the epidote skarn.

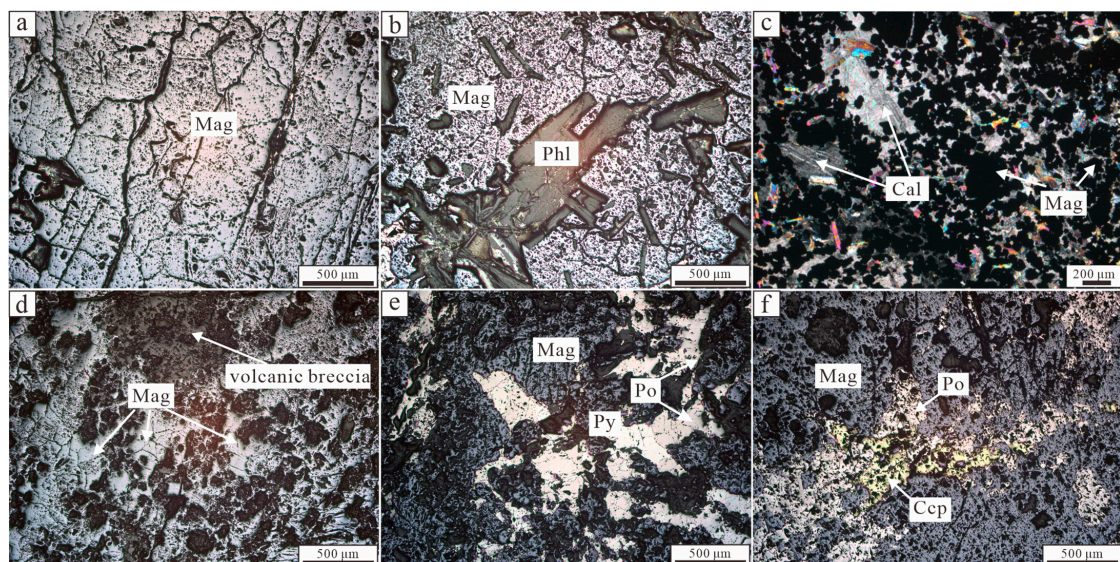


**Figure 4.** Photomicrographs showing magnetite from the Beizhan deposit. (a) Euhedral to subhedral magnetite (Mag) in massive ore. (b) Massive magnetite with interstitial phlogopite (Phl). (c) Fine-grained disseminated magnetite in calcite (Cal) veins. (d) Volcanic breccias cemented by magnetite. (e) Magnetite with interstitial pyrrhotite (Po) and pyrite (Py). (f) Magnetite that is replaced by pyrrhotite and chalcopyrite (Ccp).

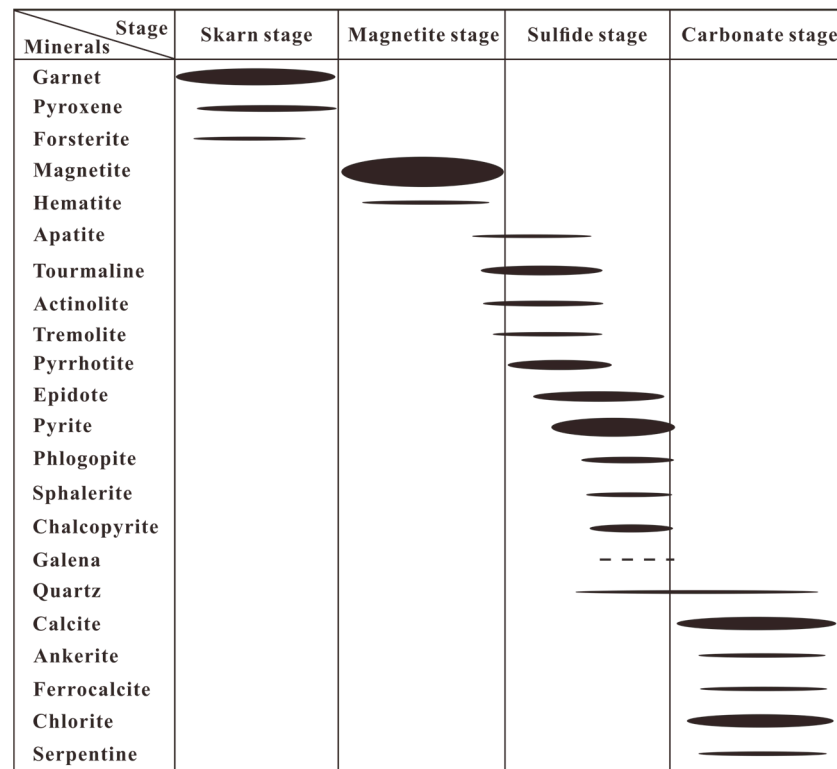


**Figure 5.** Paragenetic sequence of the Beizhan iron deposit.

#### 4. Analytical Methods

##### 4.1. Electron Microprobe Analyses

Major element analyses of magnetite were conducted utilizing a JEOL JXA-8230 electron microprobe at the Institute of Mineral Resources, Chinese Academy of Geological Sciences, Beijing. The analytical parameters were set with an acceleration voltage of 15 kV, a beam current of 20 nA, and a defocused electron beam diameter of 5  $\mu\text{m}$ . Calibration standards included both natural and synthetic minerals, including Woll MAC (Si and Ca), jadeite (Na), kyanite (K), and synthetic  $\text{TiO}_2$ ,  $\text{Fe}_2\text{O}_3$ ,  $\text{MgO}$ , and  $\text{Mn}_3\text{O}_4$ . Data reduction was executed through the ZAF correction method of the JEOL microprobe system. Analytical precision is better than 0.01%.

##### 4.2. In Situ Magnetite Trace Element Analyses

In situ trace element analyses of magnetite were completed using a high-mass-resolution Agilent 7500a ICP-MS, coupled with a New Wave UP 193SS laser ablation system at the LA-ICP-MS laboratory, China University of Geosciences, Beijing. The laser ablation system utilized a beam spot of 50  $\mu\text{m}$  and an energy beam of 8.5  $\text{J}/\text{cm}^2$ . Helium was employed as the carrier gas with a flow rate of 0.8 L/min, while argon served as the make-up gas with a flow rate of 1.15 L/min. Nitrogen gas was introduced at a flow rate of 15 L/min into the central gas flow (Ar + He) of the argon plasma to enhance detection limits and improve precision. Standard analyses were performed three times before and after each run of ten analyses to ensure accuracy and reliability. The preferred element concentration values for the USGS reference glasses were derived from the GeoReM database. External calibration was achieved using the NIST SRM 612 standard glass, while internal standardization was based on Fe. The raw data obtained from the ICP-MS instrument were exported and processed using the Glitter 4.4 software. The detection limits for most elements were considerably below 0.1 ppm.

### 4.3. Magnetite Thermometry Calculation

Canil and Lacourse [18] established a method for quantitatively estimating temperature based on the trace element concentrations of magnetite. This method, known as magnetite thermometer ( $T_{\text{Mg-mag}}$ ), utilizes Mg and Fe concentrations to express temperature as follows:

$$T_{\text{Mg-Mag}} (^{\circ}\text{C}) = -8344 (\pm 320) / [\ln X_{\text{Mg}} - 4.13 (\pm 0.28)] - 273$$

where

$$X_{\text{Mg}} = \text{Mg} / (\text{Mg} + \text{Fe}_{\text{total}})$$

The error associated with this temperature calculation is  $\pm 50$   $^{\circ}\text{C}$ . The calibration is based on the analysis of magnetite in equilibrium with fluid-saturated and undersaturated silicate melts in over 300 experiments from 27 different phase equilibrium studies, encompassing compositions ranging from basalt to granite.

### 4.4. Fe-O Isotope Analyses

Iron isotopes in magnetite were analyzed at the Iron Isotope Laboratory of the University of Science and Technology of China. Dissolution of separated magnetite crystals was carried out using 0.8 mL of high-purity hydrofluoric acid (HF) and 0.4 mL of high-purity nitric acid ( $\text{HNO}_3$ ). The analytical procedure was described in detail by Huang et al. [52]. Iron isotopic compositions were calculated using the International Atomic Energy Agency reference material IRMM-014, with the formula as follows:

$$\delta^{56}\text{Fe} = [({}^{56}\text{Fe}/{}^{54}\text{Fe})_{\text{sample}} / ({}^{56}\text{Fe}/{}^{54}\text{Fe})_{\text{IRMM-014}} - 1] \times 1000 (\text{‰})$$

The average standard deviation of sample measurements ( $2\sigma$ ) was 0.04‰.

Oxygen isotopes in magnetite were analyzed at the Key Laboratory of Isotope Geology, Ministry of Land and Resources, using a Finnigan MAT-253 mass spectrometer. Oxygen extraction followed the  $\text{BrF}_5$  analytical method as described by Clayton and Mayeda [53]. The liberated oxygen was then reacted with a hot platinized graphite rod at 700  $^{\circ}\text{C}$ , producing  $\text{CO}_2$ . Oxygen isotopic compositions were determined by analyzing the  $\text{CO}_2$  gas using a mass spectrometer. Reference materials GBW 04409 and NBS-28 were used as standards. The analytical precision for  $\delta^{18}\text{O}$  values was reported as  $\pm 0.2$ ‰ ( $2\sigma$ ). All the oxygen isotopic data were reported relative to the Vienna Standard Mean Ocean Water (V-SMOW) reference standard, following this formula:

$$\delta^{18}\text{O} = [({}^{18}\text{O}/{}^{16}\text{O})_{\text{sample}} / ({}^{18}\text{O}/{}^{16}\text{O})_{\text{VSMOW}} - 1] \times 1000 (\text{‰})$$

## 5. Results

### 5.1. Mineral Chemistry of Magnetite

The major element compositions of the three magnetite types are presented in Table 1. The  $\text{FeO}_{\text{Total}}$  content exhibits a general decreasing trend from platy magnetite and brecciated magnetite to massive magnetite, with average values of 93.53 wt.%, 93.26 wt.%, and 91.74 wt.%, respectively. In contrast, the content of  $\text{Al}_2\text{O}_3$ ; and  $\text{MgO}$  display an opposing trend, progressively increasing from platy magnetite (averaging 0.15 wt.% and 0.11 wt.%) to brecciated magnetite (averaging 0.33 wt.% and 0.30 wt.%) and finally to massive magnetite (averaging 0.79 wt.% and 0.33 wt.%). Other minor elements such as  $\text{TiO}_2$  and  $\text{Cr}_2\text{O}_3$  had low concentrations, typically less than 0.1 wt.%.

The trace element compositions of magnetite are presented in Table 2 and illustrated in Figure 6. Notably, the content of Ti and V in brecciated magnetite is about 1990 ppm and 87 ppm, respectively, which is around four times higher than those in the other two magnetite types. Likewise, the Cr, Co, and Zn contents exhibited notable enrichment in brecciated magnetite, approximately two times higher relative to those in the other magnetite varieties.

**Table 1.** Electron microprobe major element data of magnetite from the Beizhan iron deposit.

Sample	TiO <sub>2</sub>	Al <sub>2</sub> O <sub>3</sub>	TFeO	MnO	MgO	CaO	CoO	ZnO	Cr <sub>2</sub> O <sub>3</sub>	NiO	V <sub>2</sub> O <sub>3</sub>	P <sub>2</sub> O <sub>5</sub>	Total	T <sub>Mg-Mag</sub>	Type
ZK41-03-01	0	0.15	92.88	0.12	0.10	0	0.15	0	0.05	0	0.02	0	93.46	~529	Platy
ZK41-03-02	0.14	0.13	93.29	0.08	0.11	0	0.12	0.02	0.08	0	0.01	0	93.99	~537	Platy
ZK41-04-03	0.10	0.14	94.04	0.09	0.19	0	0.03	0.31	0.02	0	0	0	94.91	~581	Platy
ZK41-04-04	0.06	0.16	94.19	0.04	0.13	0	0.16	0.02	0.06	0	0	0.03	94.85	~552	Platy
ZK41-05-03	0.02	0.19	93.33	0.06	0.15	0	0.08	0.01	0.05	0	0.04	0.01	93.93	~560	Platy
ZK41-05-04	0.11	0.14	93.47	0	0.01	0	0.17	0	0.04	0	0	0.01	93.95	~403	Platy
ZK42-01-01	0.03	0.11	93.51	0.07	0.26	0	0.03	0	0.06	0	0.06	0.01	94.14	~612	Brecciated
ZK42-01-02	0	0.07	93.16	0.12	0.19	0	0.12	0.20	0.02	0	0	0	93.87	~582	Brecciated
ZK42-01-03	0.07	0.24	93.67	0.03	0.34	0	0.16	0.14	0	0	0.01	0	94.67	~637	Brecciated
ZK42-02-01	0.40	1.04	90.53	0.25	0.73	0	0.02	0.13	0.03	0	0.03	0	93.14	~723	Brecciated
ZK42-02-02	0.02	0.23	94.37	0.14	0.21	0	0.09	0	0	0	0	0	95.06	~590	Brecciated
ZK42-02-03	0.01	0.11	93.72	0.01	0.21	0	0.08	0.11	0.06	0	0	0	94.31	~592	Brecciated
ZK42-02-04	0	0.62	93.23	0.06	0.35	0	0.02	0	0	0	0	0	94.29	~641	Brecciated
ZK42-04-01	0.12	1.08	92.66	0.11	0.67	0	0.13	0.18	0.01	0	0.01	0.05	94.99	~710	Brecciated
ZK42-04-02	0.08	0.86	92.67	0.06	0.41	0	0.06	0.06	0.04	0	0	0	94.23	~656	Brecciated
ZK42-06-01	0.04	0.08	94.67	0.10	0.09	0	0.19	0.11	0.07	0	0.09	0.02	95.45	~519	Brecciated
ZK42-07-01	0	0.15	93.60	0.04	0.15	0	0.15	0	0.02	0	0.02	0	94.13	~565	Brecciated
ZK42-07-02	0	0.05	92.97	0.10	0.15	0	0.12	0.08	0	0	0.05	0	93.51	~564	Brecciated
ZK42-07-03	0.02	0.11	93.11	0.01	0.20	0	0.10	0	0.02	0	0.06	0	93.63	~587	Brecciated
ZK42-07-04	0.07	0.07	93.72	0.04	0.13	0	0.10	0	0.03	0	0.02	0	94.17	~550	Brecciated
ZK42-07-05	0	0.13	93.29	0.05	0.38	0	0.11	0	0.03	0	0.06	0	94.05	~648	Brecciated
ZK31-02-01	0	0.85	91.90	0.07	0.33	0.09	0.10	0.06	0.04	0	0	0	93.45	~636	Massive
ZK31-02-02	0	0.94	92.37	0.09	0.38	0.12	0.03	0.06	0.03	0.02	0	0.03	94.06	~649	Massive
ZK31-02-03	0.03	1.00	90.40	0	0.42	0.18	0.11	0	0.01	0	0	0	92.16	~663	Massive
ZK31-03-01	0.08	0.15	92.75	0.06	0.23	0.02	0.14	0.09	0.05	0	0.01	0	93.56	~600	Massive
ZK31-03-02	0.03	0.11	93.58	0.06	0.16	0	0.14	0.08	0.06	0	0.03	0	94.23	~566	Massive
ZK31-04-01	0.02	1.21	91.03	0.16	0.49	0.22	0.07	0.16	0.05	0	0	0.02	93.41	~678	Massive
ZK31-04-02	0.01	1.05	91.63	0.05	0.37	0.17	0.11	0	0.02	0	0	0	93.42	~648	Massive
ZK31-05-01	0.04	0.01	94.75	0.04	0	0	0.07	0.11	0.05	0	0	0.01	95.08	/	Massive
ZK31-05-02	0.03	0.93	91.26	0.02	0.31	0.07	0.08	0.06	0.03	0	0.02	0.01	92.83	~631	Massive
ZK31-05-03	0.08	1.09	90.09	0.08	0.47	0.15	0.20	0.25	0.04	0	0.05	0	92.49	~673	Massive
ZK31-06-01	0.03	1.11	89.33	0.02	0.46	0.15	0.05	0.19	0.04	0	0	0.01	91.37	~672	Massive
ZK31-06-02	0.08	0.97	91.83	0	0.34	0.08	0.06	0.10	0.04	0	0	0.01	93.50	~639	Massive

**Table 2.** LA-ICP-MS trace element data of magnetite from the Beizhan iron deposit.

Sample	Sc	Ti	V	Cr	Co	Ni	Cu	Zn	Ga	Zr	Nb	Mo	Sn	Hf	Ta	Type
ZK41-03-01	0.64	282.46	7.65	9.38	5.60	2.20	0.26	418.03	9.70	1.22	0.96	0.20	6.82	0.38	0.07	Platy
ZK41-03-02	0.53	176.53	7.45	7.71	7.28	2.93	0.30	697.60	11.05	0.36	0.99	0.25	8.13	0.26	0.09	Platy
ZK41-03-03	0.44	336.39	10.14	10.89	6.52	2.85	0.34	941.90	13.82	0.47	0.83	0.23	7.34	0.37	0.08	Platy
ZK41-04-01	0.53	421.53	30.41	38.45	6.82	2.81	0.29	613.17	11.60	0.43	0.46	0.20	5.43	0.24	0.10	Platy
ZK41-04-02	0.47	466.02	29.53	6.81	5.86	2.35	0.24	136.21	10.38	0.18	0.31	0.26	2.80	0.20	0.07	Platy
ZK41-04-03	0.33	442.89	25.74	19.50	73.71	35.00	517.02	26.69	8.92	0.11	0.14	0.21	2.12	0.18	0.06	Platy
ZK41-05-01	0.39	473.04	12.40	3.30	10.79	2.10	0.29	882.64	10.87	0.53	0.50	0.26	7.13	0.35	0.11	Platy

Table 2. Cont.

Sample	Sc	Ti	V	Cr	Co	Ni	Cu	Zn	Ga	Zr	Nb	Mo	Sn	Hf	Ta	Type
ZK41-05-02	0.50	662.30	34.76	4.56	4.17	1.75	0.37	49.58	9.81	0.34	0.74	0.24	3.91	0.31	0.10	Platy
ZK41-05-03	0.46	730.17	41.72	4.14	4.35	1.40	1.21	616.72	10.07	0.38	0.72	0.28	5.65	0.35	0.11	Platy
ZK41-06-01	0.51	571.12	20.53	3.24	9.97	2.13	0.37	128.27	10.23	0.31	0.48	0.22	5.28	0.25	0.07	Platy
ZK41-06-02	0.29	428.32	11.61	4.74	5.30	2.11	0.30	922.96	10.20	0.57	0.48	0.24	7.64	0.23	0.07	Platy
ZK41-06-03	0.48	555.79	13.24	13.54	6.89	2.13	1.45	152.03	17.23	0.50	1.00	0.27	5.69	0.32	0.10	Platy
ZK42-02-01	0.34	1146.47	72.52	19.77	6.13	2.04	0.75	635.54	16.08	1.35	0.12	0.53	12.01	0.54	0.11	Brecciated
ZK42-02-02	0.38	1736.27	96.88	7.26	6.59	1.34	9.91	502.35	15.21	0.90	0.12	0.35	7.15	0.46	0.18	Brecciated
ZK42-02-03	0.37	1018.27	65.96	5.49	7.23	1.39	0.64	1133.63	16.24	1.37	0.34	0.35	10.80	0.48	0.17	Brecciated
ZK42-02-04	0.40	3603.95	101.89	47.09	10.75	1.49	0.67	2262.27	19.76	1.12	0.76	0.56	13.75	0.43	0.13	Brecciated
ZK42-02-05	0.39	3189.08	118.26	7.67	7.54	1.93	0.54	277.54	13.23	0.84	0.58	0.29	8.17	0.51	0.13	Brecciated
ZK42-04-01	0.44	2983.27	87.77	184.77	134.20	1.68	4.95	634.58	13.39	0.86	0.45	0.26	9.19	0.27	0.10	Brecciated
ZK42-04-02	0.27	1786.39	80.94	15.52	18.70	1.61	1.99	593.40	13.50	0.56	0.41	0.22	9.31	0.38	0.09	Brecciated
ZK42-04-03	0.48	2044.46	79.23	6.32	36.13	1.62	0.58	501.83	13.39	0.54	0.25	0.25	6.97	0.36	0.09	Brecciated
ZK42-07-01	0.33	1210.06	85.46	19.06	9.09	1.95	9.59	202.70	11.93	0.47	0.22	0.31	7.51	0.36	0.11	Brecciated
ZK42-07-02	0.44	2053.26	92.67	13.08	8.02	1.50	0.48	784.53	12.84	0.41	0.21	0.34	9.00	0.57	0.10	Brecciated
ZK42-07-03	0.57	1217.75	93.59	22.26	6.55	1.30	4.93	107.02	12.36	0.97	0.41	0.33	11.21	0.50	0.14	Brecciated
ZK42-07-04	0.43	1744.03	78.77	27.95	9.71	1.59	0.54	1068.63	14.67	0.76	0.28	0.53	10.68	0.48	0.19	Brecciated
ZK42-08-01	0.28	1284.94	73.94	3.67	6.86	1.32	27.21	904.37	13.37	0.99	0.53	0.28	9.80	0.32	0.08	Brecciated
ZK42-08-02	0.43	3415.51	90.62	3.25	9.70	2.60	98.65	643.39	13.27	4.03	4.15	0.26	20.10	0.39	0.30	Brecciated
ZK42-08-03	0.34	2035.45	93.64	3.34	7.82	1.89	0.38	1013.83	13.44	0.58	0.30	0.27	9.64	0.30	0.08	Brecciated
ZK42-08-04	0.29	1377.26	78.73	5.53	9.18	1.92	29.14	925.35	13.23	0.63	0.28	0.28	10.02	0.35	0.10	Brecciated
ZK31-02-01	0.51	458.74	9.84	3.39	3.14	3.59	0.39	287.80	7.16	4.69	1.48	0.17	10.61	0.38	0.07	Massive
ZK31-02-02	0.41	389.33	5.77	2.78	5.07	3.42	0.24	836.37	7.67	5.29	1.42	0.18	12.14	0.24	0.07	Massive
ZK31-02-03	0.50	366.19	5.52	3.27	4.80	4.12	0.27	829.07	7.40	4.67	1.47	0.21	12.22	0.33	0.06	Massive
ZK31-02-04	0.41	334.47	7.11	3.72	3.76	4.04	0.44	403.96	9.29	4.69	2.09	0.30	16.03	0.30	0.09	Massive
ZK31-03-01	1.19	592.44	22.44	5.42	1.84	0.65	0.23	26.54	4.83	6.99	6.78	0.16	13.79	0.24	0.09	Massive
ZK31-03-02	0.80	528.51	20.16	38.63	2.70	0.79	0.69	49.77	6.53	7.13	6.56	0.15	16.32	0.16	0.17	Massive
ZK31-03-03	0.26	316.14	24.04	5.79	3.02	0.77	0.29	25.73	4.23	0.99	0.92	0.24	4.75	0.26	0.09	Massive
ZK31-03-04	0.76	811.66	48.73	10.25	4.17	1.79	1.06	46.38	10.17	4.90	2.37	0.49	12.12	0.56	0.17	Massive
ZK31-04-01	0.64	271.96	9.26	3.03	2.89	4.09	0.37	193.31	9.52	6.68	3.14	0.21	21.33	0.27	0.09	Massive
ZK31-04-02	0.32	183.61	7.27	3.76	3.67	4.07	0.35	649.99	9.14	1.92	1.41	0.24	14.37	0.27	0.10	Massive
ZK31-04-03	2.33	848.01	26.11	12.04	10.44	10.73	1.10	990.74	32.26	14.37	7.71	0.71	61.43	0.99	0.28	Massive
ZK31-04-04	0.37	136.42	6.79	2.57	4.46	3.17	0.28	244.20	8.37	3.95	1.61	0.16	15.32	0.28	0.07	Massive
ZK31-05-01	0.38	968.21	48.69	5.13	11.80	3.73	0.94	70.64	13.30	1.35	0.11	0.35	7.01	0.40	0.09	Massive
ZK31-05-02	0.21	584.19	27.25	1.81	6.20	1.60	0.27	184.03	7.27	0.30	0.38	0.11	5.59	0.11	0.05	Massive
ZK31-05-03	0.18	465.31	21.58	3.02	5.43	1.71	0.49	50.42	7.20	1.16	0.14	0.14	2.70	0.16	0.06	Massive
ZK31-05-04	0.31	501.09	42.54	3.78	3.99	1.36	0.25	67.35	6.41	3.03	0.52	0.19	4.75	0.18	0.06	Massive
ZK31-05-05	0.25	516.80	25.82	5.63	2.14	1.55	0.93	81.81	6.81	4.00	0.26	0.18	4.46	0.19	0.06	Massive
ZK31-06-01	0.31	348.29	13.23	4.77	2.62	2.83	0.19	285.45	5.52	2.09	0.58	0.12	7.67	0.22	0.04	Massive
ZK31-06-02	1.27	566.77	24.74	10.79	10.42	10.15	0.82	212.52	25.45	14.48	5.17	0.57	43.15	0.84	0.22	Massive
ZK31-06-03	0.21	81.93	6.33	2.58	3.69	3.59	0.22	294.73	7.74	2.07	1.20	0.15	12.27	0.23	0.08	Massive
ZK31-06-04	0.28	85.20	6.16	2.91	3.94	3.11	0.29	603.86	7.33	4.05	1.67	0.25	15.06	0.22	0.06	Massive

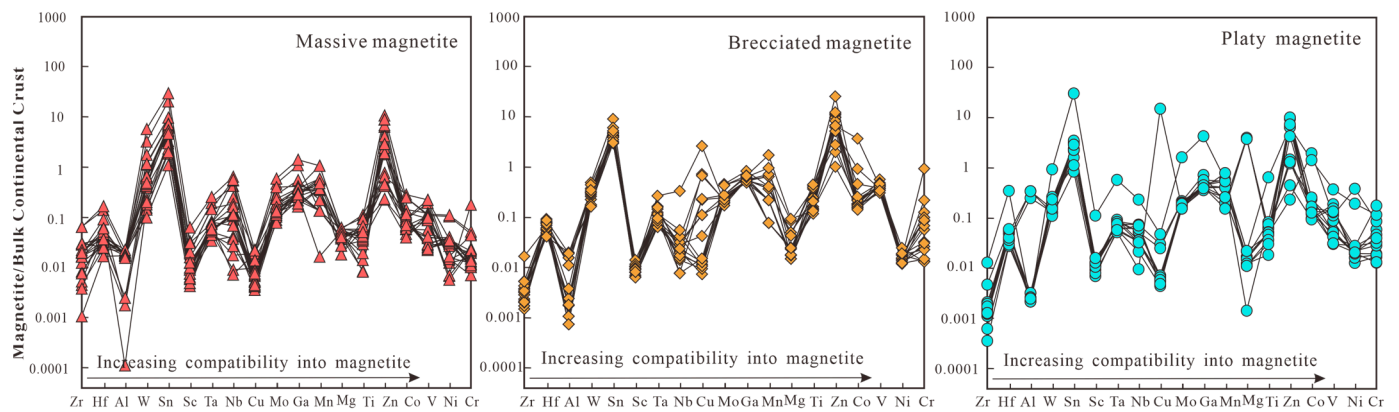


**Figure 6.** Bulk continental crust-normalized multielement plots of magnetite from the Beizhan iron deposit. Bulk continental crust values are from [54]; the order of elements is in accordance with the increasing compatibility with magnetite [55].

In contrast, platy magnetite displayed the highest Cu content, while the Sr content was predominantly enriched in massive magnetite. For the remaining trace elements, no significant differences were observed among the various magnetite types. The rare earth element content across the different magnetite types was relatively modest; however, brecciated magnetite showed a narrow concentration range, while platy magnetite exhibited slightly greater variability. Massive magnetite demonstrated the most extensive variations compared to the other two magnetite types.

5.2. Precipitation Temperature of Magnetite

The precipitation temperatures of various magnetite types from the Beizhan deposit are illustrated in Figure 7a. Additionally, the average concentrations of Ti, V, and Ga in these magnetite types are plotted in Figure 7b. The calculated temperatures for magnetite precipitation in the Beizhan deposit span a range from approximately 403 °C to 723 °C. Specifically, the massive and brecciated magnetite yield a similar temperature range, spanning approximately 566 to 678 °C (with an average of 612 °C) and 519 to 723 °C (with an average of 641 °C), respectively, both higher than those of platy magnetite, ranging from approximately 403 to 581 °C, with an average of 552 °C (except for an erratic value of 403 °C).

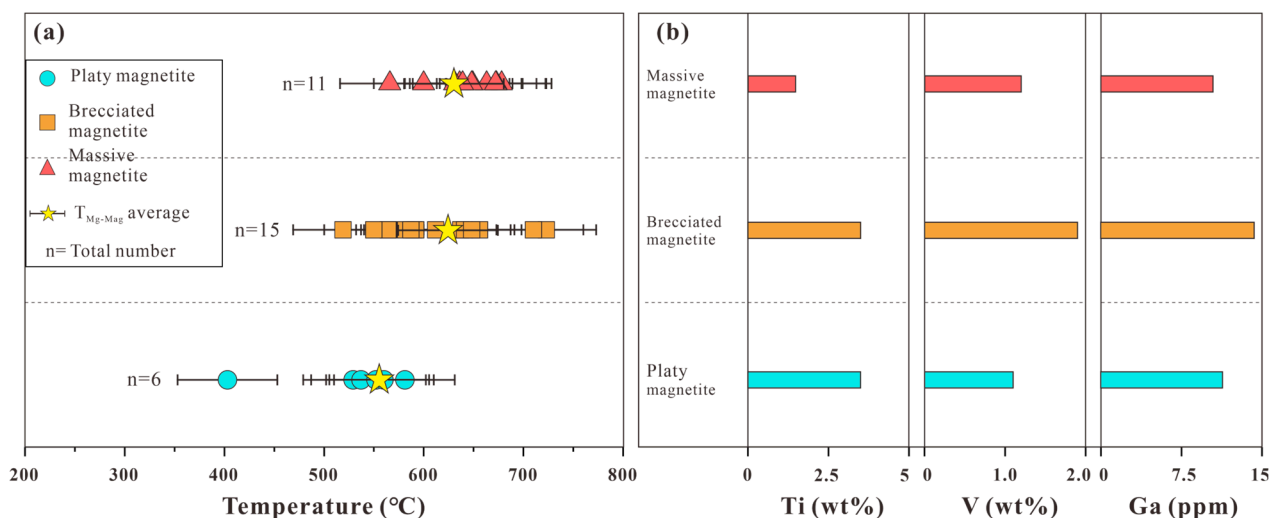


**Figure 7.** (a) Calculated temperatures and (b) median concentrations of selected trace elements in magnetite from the Beizhan iron deposit. Temperatures were calculated using the  $T_{Mg-mag}$  thermometer. Uncertainties (error bar) in  $T_{Mg-mag}$  are at  $\pm 50$  °C.

### 5.3. Fe-O Isotopic Composition of Magnetite

The Fe-O isotopic compositions of various magnetite types from the Beizhan iron deposit are provided in Table 3 and Figure 8a,b. For the brecciated ores, the  $\delta^{56}\text{Fe}$  values range from  $-0.178\text{‰}$  to  $-0.015\text{‰}$ , with an average value of  $-0.073\text{‰}$ . The massive ores exhibited  $\delta^{56}\text{Fe}$  values of  $-0.078\text{‰}$  to  $+0.005\text{‰}$ , with an average value of  $-0.049\text{‰}$ . Platy ores displayed  $\delta^{56}\text{Fe}$  values of  $+0.177\text{‰}$  to  $+0.200\text{‰}$ , averaging at  $+0.189\text{‰}$ .

**Table 3.** Iron and oxygen isotope compositions of magnetite from the Beizhan iron deposit.

Sample	$\delta^{56}\text{Fe}_{\text{IRMM-014}}$ (‰)	$\delta^{57}\text{Fe}_{\text{IRMM-014}}$ (‰)	$\delta^{18}\text{O}_{\text{V-SMOW}}$ ‰	Ore Type	Data Source
ZK34	-0.015	-0.001	1.2	Brecciated magnetite	This study
ZK-35	-0.178	-0.260	2.3	Brecciated magnetite	This study
ZK-28	-0.025	-0.077	4.5	Brecciated magnetite	This study
ZK-33	-0.074	-0.100	2.4	Massive magnetite	This study
ZK-31	0.005	-0.026	2.5	Massive magnetite	This study
ZK-40	-0.078	-0.122	4.6	Massive magnetite	This study
14WBZ-14	-0.047	-0.160	1.5	Massive magnetite	This study
ZK-39	0.200	0.283	0.6	Platy magnetite	This study
ZK-41	0.177	0.289	2.7	Platy magnetite	This study
bei10	-0.065	-0.096	-	Vein magnetite	Wang [56]
bei14	-0.120	-0.177	-	Vein magnetite	Wang [56]
bei15	-0.121	-0.178	-	Vein magnetite	Wang [56]
bei19	0.018	0.027	-	Massive magnetite	Wang [56]
bei20	-0.061	-0.090	-	Massive magnetite	Wang [56]
11BZ-32	-0.181	-0.267	-	Vein magnetite	Wang [56]
ZK702-278.5	-	-	5.2	-	Yang et al. [17]
BZ-001	-	-	5.0	-	Yang et al. [17]
BZ-8t-1	-	-	4.9	-	Yang et al. [17]
BZ-1t-1	-	-	5.3	-	Yang et al. [17]
ZK005-655.2	-	-	2.4	-	Yang et al. [17]

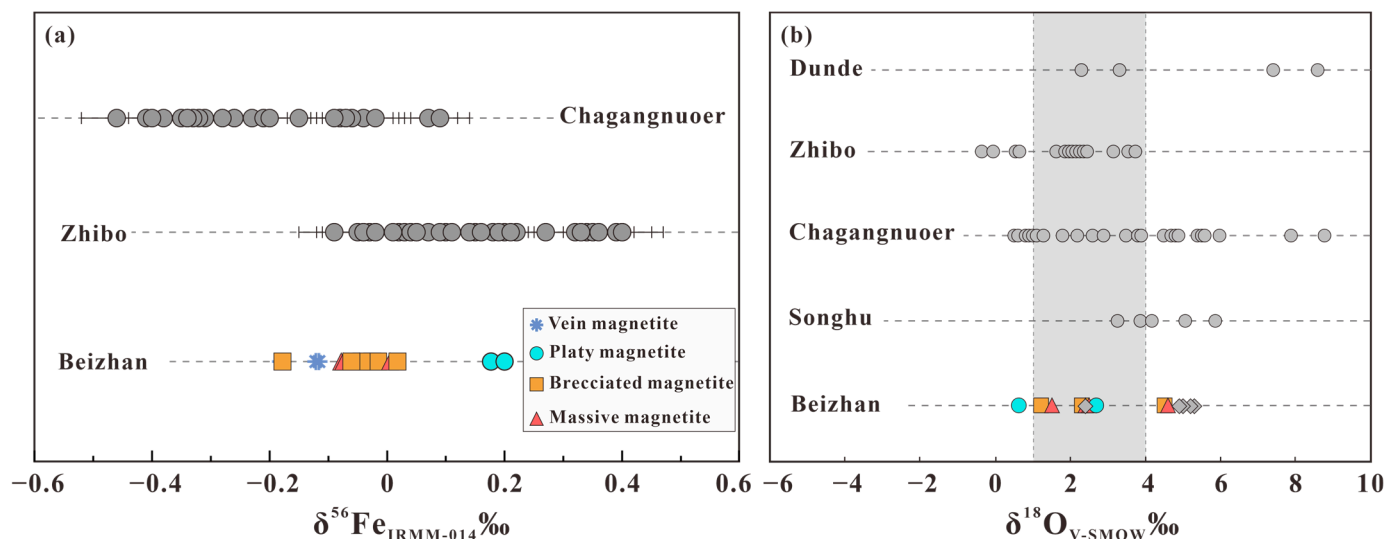


**Figure 8.** Comparison of (a) Fe isotopic and (b) O isotopic compositions for magnetite from the Beizhan deposit with other iron deposits in the AIMB. Also included are  $\delta^{56}\text{Fe}$  values [56] and  $\delta^{18}\text{O}$  values (gray diamonds) [17] for magnetite from the Beizhan deposit. The  $\delta^{56}\text{Fe}$  ranges for the Zhibo and Chagangnuoer iron deposits are from [12,56]. The  $\delta^{18}\text{O}$  ranges for the Dundee, Zhibo, Chagangnuoer, and Songhu iron deposits are from [17,33,35,36,57–59].

The  $\delta^{18}\text{O}$  values of magnetite exhibited notable variations, ranging from  $+0.6\text{‰}$  to  $+4.6\text{‰}$ . Specifically, the  $\delta^{18}\text{O}$  values of three brecciated magnetite samples were  $+1.2\text{‰}$ ,

+2.4‰, and +4.5‰, with an average value of +2.7‰. The  $\delta^{18}\text{O}$  values of four massive magnetite samples were +1.5‰, +2.4‰, +2.5‰, and +4.6‰, with an average of +2.8‰. Platy magnetite samples exhibited  $\delta^{18}\text{O}$  values of +0.6‰ and +2.7‰, with an average of +1.7‰.

## 6. Discussion

### 6.1. Origin of the Beizhan Magnetite

The magnetite in the Beizhan deposit contains significantly lower contents of  $\text{TiO}_2$ ,  $\text{Cr}_2\text{O}_3$ , and  $\text{V}_2\text{O}_5$  compared to iron deposits formed through magmatic processes, such as Kiruna-type and Chilean-type iron ore deposits. In the Al+Mn vs. Ti+V diagram (Figure 9a,c) [60], the massive magnetite samples predominantly cluster within the skarn magnetite deposit region, revealing constrained contents of Ti, V, Al, and Mn [61]. Conversely, in the case of platy ores, magnetite more closely aligns with IOCG-type and skarn-type magnetite deposit regions. These platy magnetite grains exhibit lower trace element contents, the incorporation of which into the magnetite structure appears to be temperature-dependent. This observation implies that the genesis of this magnetite type may be associated with lower-temperature hydrothermal processes [61].

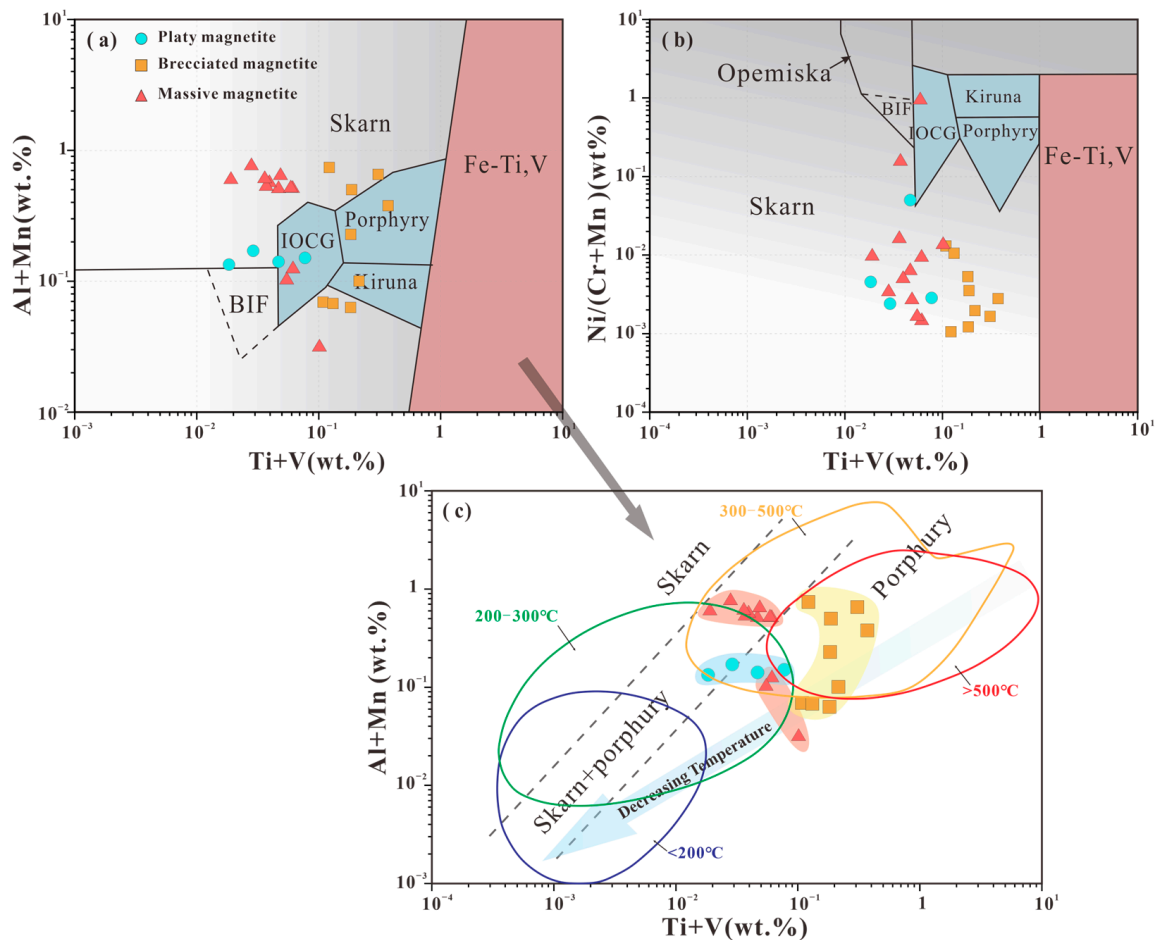


**Figure 9.** Discrimination diagram of (a,c) Al + Mn vs. Ti + V and (b) Ni/(Cr + Mn) vs. Ti + V for magnetite from the Beizhan iron deposit (after [60] and modified by [62]). The different fields of temperature are adapted from [63,64].

Magnetite in the brecciated ores exhibit a broad distribution, suggesting a more complex and diverse origin. Similarly, in the Ni/(Cr+Mn) vs. Ti+V diagram (Figure 9b), the measured points of magnetite grains show relatively low Ti+V concentrations and low Ni/(Cr+Mn) values, indicating a skarn type. These characteristics align with hydrothermal

genetic features, which are further corroborated in the Ti vs. V diagram (Figure 10a). In the Ti vs. Ni/Cr diagram (Figure 10b), the magnetite data extend across both hydrothermal and magmatic origin fields, implying that the magnetite in the Beizhan deposit carries information related to both hydrothermal and magmatic origins.

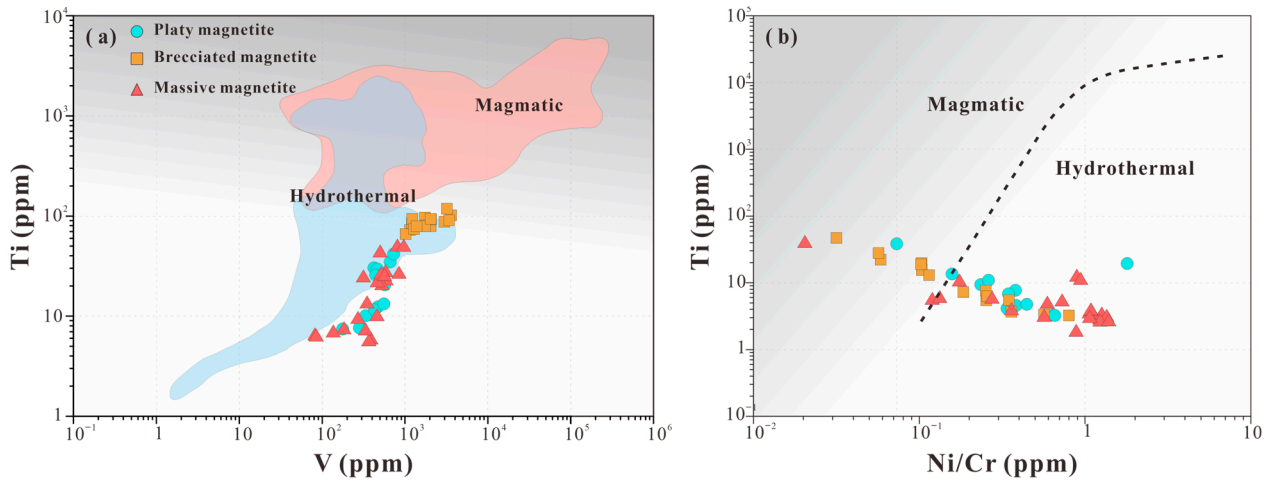


**Figure 10.** Discrimination diagram of (a) Ti vs. V and (b) Ni/Cr vs. Ti for magnetite from the Beizhan iron deposit. Fields of magmatic and hydrothermal magnetite are from [62,65,66].

The higher concentrations of Ti and Cr observed in brecciated magnetite are indicative of early crystallization compared to the other two types of magnetite, as both Ti and Cr are considered compatible elements within magnetite (Figure 11a). In addition, in magmatic deposits, there is typically a coupling relationship between Ni and Cr, with Ni/Cr ratios mostly being  $\leq 1$ . These patterns in the element distribution characteristics within the magnetite suggest that the formation of magnetite in the Beizhan deposit is not solely the result of magmatism (Figure 11b). Instead, it is likely that the genesis of magnetite is linked to magmatic–hydrothermal fluid processes.

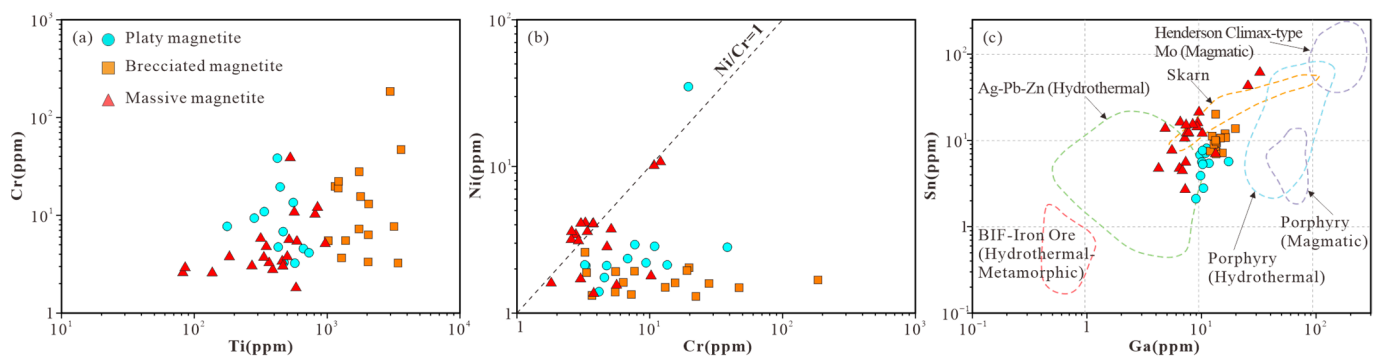


**Figure 11.** Binary diagrams of (a) Cr vs. Ti, (b) Ni vs. Cr, (c) Sn vs. Ga for magnetite from the Beizhan iron deposit, the different types magnetite from the typical porphyry (magmatic), porphyry (hydrothermal), skarn, Ag-Pb-Zn (hydrothermal), and BIF-iron ore (hydrothermal–metamorphic) [64,67].

Furthermore, the content of Sn can serve as an additional petrogenetic indicator, with Sn and Ga concentrations having been proposed for distinguishing between low- and high-temperature hydrothermal and magmatic magnetite [64,67]. The magnetite plots within the hydrothermal regions, specifically across the Ag-Pb-Zn hydrothermal and skarn hydrothermal fields, are shown in the Sn vs. Ga diagram (Figure 11c). This further underscores a hydrothermal source for the magnetite. Taken together, these findings collectively suggest a complex origin for the Beizhan deposit, one that involves the interaction of magmatic and hydrothermal fluids in its formation.

The trace element distribution characteristics, particularly the low Ti content, in magnetite from the Beizhan iron deposit exhibit significant distinctions from typical magnetite deposits formed by magmatic processes, such as Fe-Ti-V deposits and Fe-Ti-P deposits. However, these characteristics bear a resemblance to those of hydrothermal deposits, specifically IOA-type and Porphyry-type deposits (Figure 12). A comparison of the element distribution characteristics in Beizhan deposit magnetite with those found in hydrothermal deposits reveals a consistent trend. Magnetite in the Beizhan iron deposit is notably enriched in immobile elements like Zr, Hf, Zn, Co, Sc, and others, elements commonly associated with hydrothermal fluids. Conversely, the magnetite displays depletion in highly incompatible elements like Si, Ca, and so forth, which are typically linked with magmatic magnetite deposits.

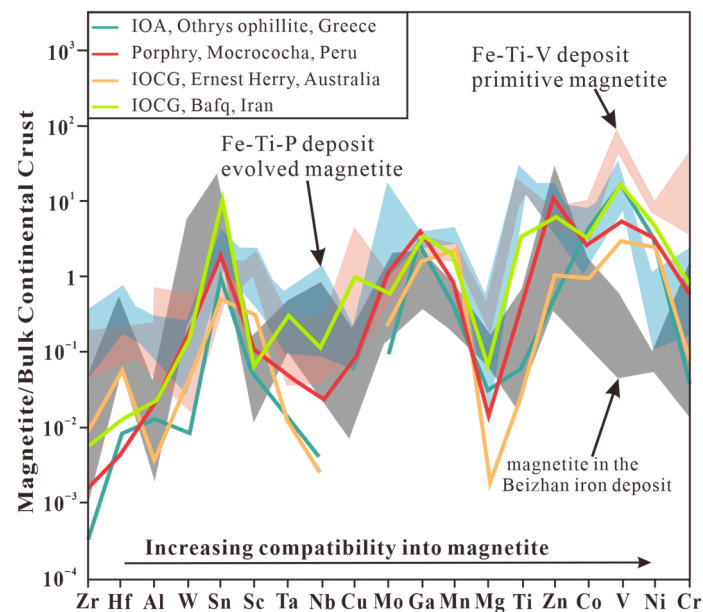


**Figure 12.** Bulk continental crust-normalized multi-element plots of magnetite from the Beizhan iron deposit. Data fields are taken from [68]. Bulk continental crust values are from [54].

These findings further support the interpretation that the Beizhan deposit has undergone a hydrothermal overprint. The enrichment of immobile elements and the depletion of incompatible elements in the magnetite provide evidence that the formation of the Beizhan iron deposit is closely linked with hydrothermal processes, rather than being solely attributed to a magmatic origin.

## 6.2. Thermal Evolution of the Mineralization

Application of the Mg-in magnetite thermometer ( $T_{\text{Mg-mag}}$ ) reveals a substantial temperature discrepancy among different magnetite types within the Beizhan deposit. Specifically, it indicates that massive and brecciated magnetite crystallized at higher temperatures, with averages of approximately 641 °C and 612 °C, respectively, while platy magnetite exhibits a relatively lower crystallization temperature, averaging around 552 °C (Figure 7a, Table 1). This decreasing temperature trend correlates with trace element concentrations such as Ti, V, and Ga. These elements demonstrate elevated levels in deposits with a predominantly hydrothermal origin, while they exhibit comparatively reduced levels in deposits associated with magmatic or magmatic–hydrothermal sources (Figure 7b). The Al+Mn vs. Ti+V diagram (Figure 9c) further reflects this changing trend in the formation temperature of magnetite, with magnetite plots consistent with the gradual decrease in temperatures from brecciated and massive to platy magnetite.

A combination of magmatic and hydrothermal processes, as revealed by  $T_{\text{Mg-mag}}$ , helps elucidate the thermal evolution of the Beizhan deposit (Figure 13). The earlier

brecciated magnetite and the following massive magnetite exsolved in stage 2 and stage 3 (at temperatures around 800 to 600 °C and below 600 °C, respectively) as a result of cooling alongside the Fe-rich magmatic–hydrothermal fluid. The latest platy magnetite precipitated from low-temperature hydrothermal fluids in stage 3 (<600 °C), which mostly occurs with the injection of fluids, leading to complex magnetite growth and pervasive replacement horizons [69].

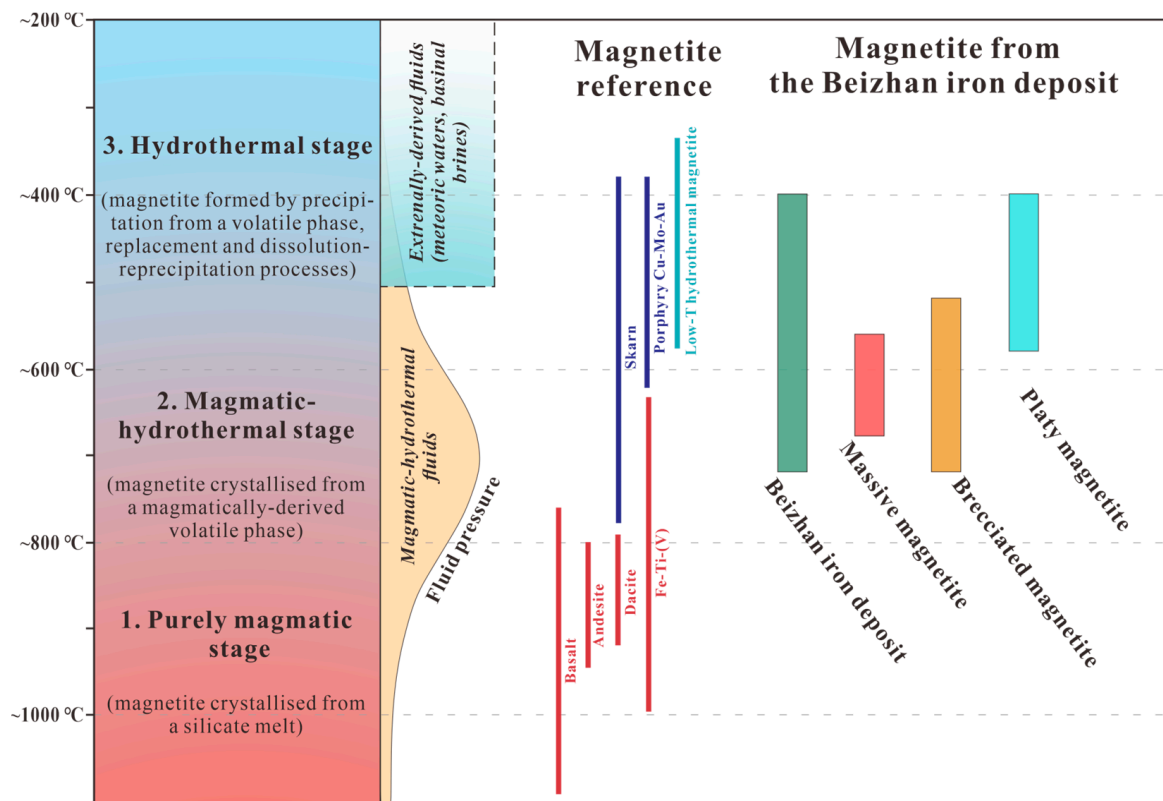


**Figure 13.** Thermal evolution of the Beizhan iron deposit. Reference temperatures of magnetite from various volcanic rocks and deposits, and magmatic to hydrothermal stages are from [70] and [69].

In summary, the thermal evolution of the Beizhan deposit can be reconstructed by the magnetite thermometry ( $T_{\text{Mg-mag}}$ ), which provides a quantitative estimation of cooling trends in variable types of ores. It delineates a transition from magmatic or magmatic–hydrothermal conditions (massive and brecciated ore) to purely hydrothermal conditions (platy ore).

### 6.3. Source of Ore Components

Previous studies have demonstrated that the iron isotopic system is susceptible to isotopic fractionation during the Earth's magmatic processes [71–74]. During the partial melting of the mantle, iron isotopes tend to be incompatible and are concentrated in silicate minerals and magmas [75,76]. Knipping et al. [3] suggested that light Fe isotopes are predominantly enriched in fluid, while heavy Fe isotopes are enriched in magmatism. The marked variation in Fe isotopic compositions of magnetite from the Beizhan deposit indicates substantial fractionation of Fe isotopes during the formation of magnetite ores. The  $\delta^{56}\text{Fe}$  values of massive (−0.078 to +0.005‰) and brecciated (−0.178 to −0.015‰) magnetites closely resemble those of Fe-skarn magnetites found in hydrothermal Fe deposits, such as the Dannemora (−0.43 to +0.01‰) [77], Xinqiao (−0.37 to +0.13‰) [78], and Changanuoer deposits (−0.40 to +0.10‰) [12] and the Zankan Fe deposit (−0.30 to +0.50‰) [79]. This suggests a similar lighter magmatic–hydrothermal fluid source for the massive and brecciated magnetite ores.

In contrast, the Fe isotopic composition of platy (+0.177 to +0.200‰) magnetite, which is interpreted as having a low-T hydrothermal crystallization history based on its trace element behavior and magnetite thermometry, significantly deviates from the  $\delta^{56}\text{Fe}$  range of magmatic/high-T origin (Figure 14). Mineral assemblages and paragenetic relationships suggest that sulfides formed after magnetite precipitation. Platy magnetite often occurs together with pyrrhotite, which possesses the lightest Fe isotope composition in Fe skarn deposits [80]. The precipitation of pyrrhotite causes the fluid to become enriched in heavy Fe isotopes, and the subsequently precipitated platy magnetite thus has a heavier Fe isotopic composition. The formation of hydrothermal magnetite in skarn deposits is commonly associated with the dissolution–reprecipitation process [81,82]. During such a process, the primary magnetite may exchange Fe isotopes with the fluid, whose Fe isotopic composition is influenced by the pathways of pyrrhotite formation.

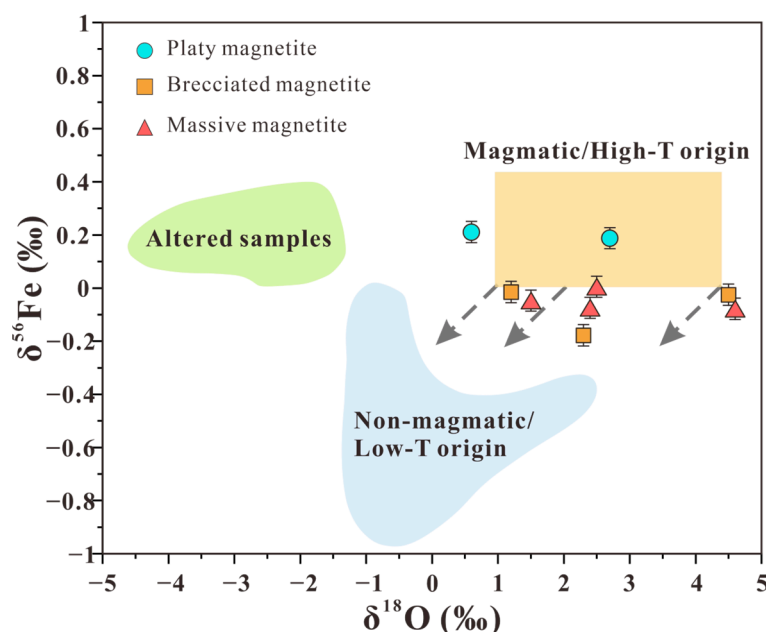


**Figure 14.**  $\delta^{56}\text{Fe}$  vs.  $\delta^{18}\text{O}$  diagram for magnetite from the Beizhan iron deposit (modified from [6]). The orange box denotes the isotope ranges of magmatic or high-T origin [68,70,77,83,84].

Considerable research has focused on the variability in  $\delta^{18}\text{O}$  values of magnetite from different ore types of iron deposits, indicating the potential for using  $\delta^{18}\text{O}$  values to distinguish deposit types and infer their genesis [17,56,59,85,86]. Magnetite formed through magmatism typically exhibits a relatively narrow range of  $\delta^{18}\text{O}$  values, usually falling between +1‰ and +4‰ [5,59,70,83,87]. Oxygen isotope analyses of magnetite samples extracted from different types of iron ore in the Beizhan iron deposit (massive, brecciated, and platy type) predominantly yield  $\delta^{18}\text{O}$  values ranging from +0.6 to +4.6‰, which are highly consistent with those of magnetites found in the iron oxide deposits in the AIMB (Zhibo, Chagangnuoer, and Songhu iron deposits) [35,36]. Furthermore, these  $\delta^{18}\text{O}$  values closely resemble those observed in the El Laco and Kiruna deposits (Figure 15) [5,7,8,10,70,87].

Magnetite samples with  $\delta^{18}\text{O}$  values ranging between +0.9 and +4.0‰ are typical for magnetite that is in equilibrium with intermediate to felsic magmas or magmatic fluids at high temperatures (~800–1000 °C; i.e., ortho-magmatic magnetite), while values below +0.9‰ are indicative of hydrothermal fluids at low temperatures [12,87]. Most of the magnetite samples from the Beizhan deposit, except for one massive magnetite with a  $\delta^{18}\text{O}$  less than +0.9‰ and two magnetite samples (brecciated and platy magnetite) with values greater than +4.0‰ that exhibit  $\delta^{18}\text{O}$  values between +0.9‰ and +4.0‰, classifying them as ortho-magmatic magnetite. This suggests that they were in equilibrium with magmas or

magmatic fluids at high temperatures. The prevalence of hydrothermal alterations in the Beizhan iron deposit supports the superposition of low-temperature hydrothermal fluids in the late stage, contributing to the modification of the magnetite formed in the early stage.

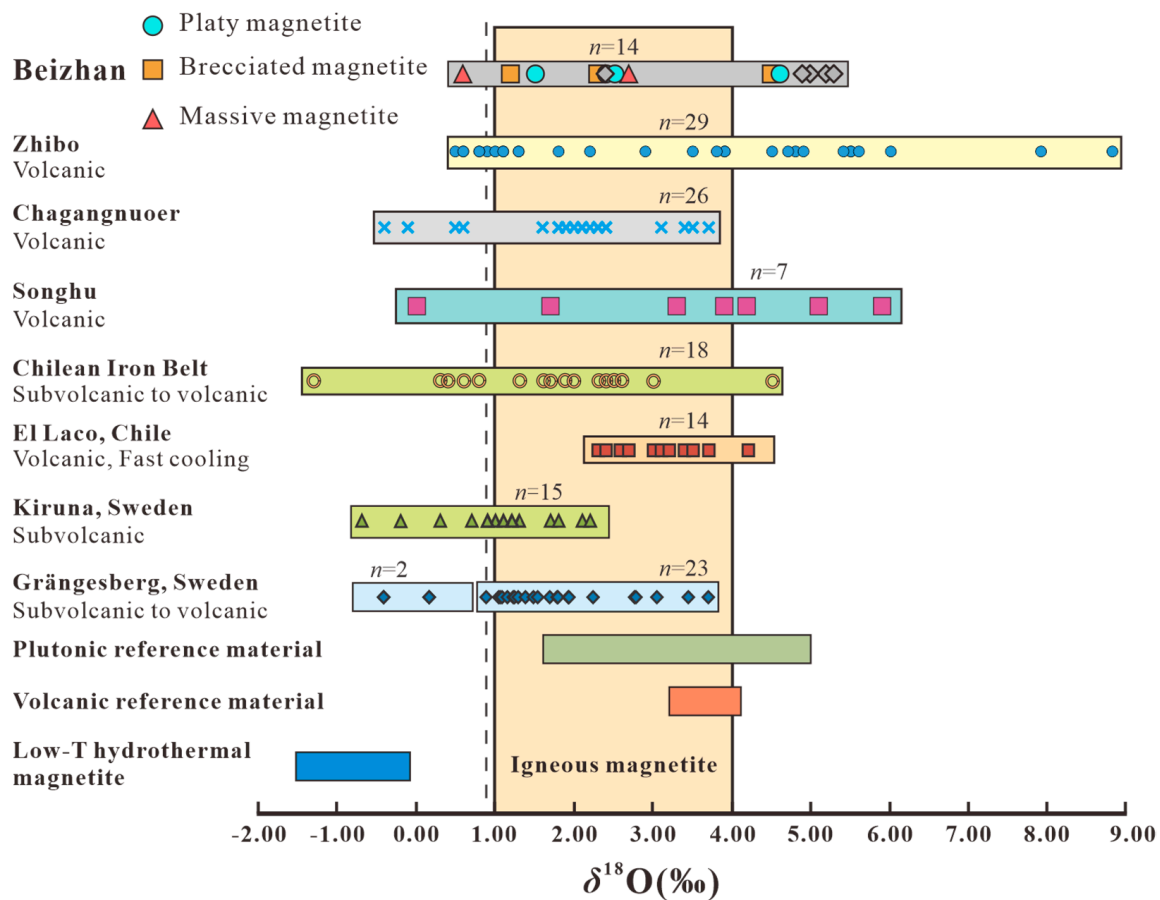


**Figure 15.** Comparison of  $\delta^{18}\text{O}$  values for magnetite from the Beizhan iron deposit with other volcanic-hosted iron deposits. Also included are  $\delta^{18}\text{O}$  values (gray diamonds) for magnetite from the Beizhan deposit [17]. Data of Zhibo, Changanuoer, and Songhu iron deposits are from [17,33,35,36,38,57]. Data of Chilean iron belt, El Laco, Kiruna, and Grängesberg, are from [7,87]. Range of plutonic material, volcanic material, and low-T hydrothermal magnetite are from [70]. The cutoff line at  $\delta^{18}\text{O} = +0.9\text{‰}$  demarcates magnetite derived from silicate magma or magmatic–hydrothermal fluid [7,8]. The yellow box (+1 to +4‰) is typical  $\delta^{18}\text{O}$  values for ortho-magmatic magnetite [10,68].

The  $\delta^{18}\text{O}$  data strongly support the idea of a magmatic–hydrothermal origin with a dominance of hydrothermal processes. This hypothesis is further reinforced by the trace element signature of the magnetite and the extensive evidence of hydrothermal alterations within the Beizhan iron deposit. The prevalence of low-temperature hydrothermal fluids in the late stage appears to have played a significant role in modifying the magnetite formed during the early stages of deposit formation.

### 7. Conclusions

The in situ LA-ICP-MS magnetite trace element composition in the Beizhan deposit suggests a complex origin involving the interaction of both magmatic and hydrothermal fluids. The trace element distributions, particularly Ti, V, Sn, Ga, Ni, Cr, etc., coupled with the enrichment of immobile elements and depletion of incompatible elements, indicates the involvement of magmatic–hydrothermal processes in the formation of the Beizhan deposit.

Utilizing magnetite thermometry ( $T_{\text{Mg-mag}}$ ) to determine crystallization temperatures for the three ore types, our findings reveal a significant temperature difference between the

relatively higher-temperature brecciated magnetite (average ~641 and 612 °C, respectively) and the relative lower-temperature platy magnetite (average ~552 °C). This temperature discrepancy indicates a cooling trend and signifies a transition from magmatic or magmatic–hydrothermal conditions (as observed in massive and brecciated ore) to purely hydrothermal conditions in the case of platy ore.

Stable Fe and O isotope values of magnetite from the Beizhan deposit shed light on the source of ore-forming materials. The  $\delta^{56}\text{Fe}$  values for brecciated and massive magnetite fall within the ranges  $-0.178$  to  $+0.005\%$ , indicating a magmatic–hydrothermal reservoir. However, the  $\delta^{56}\text{Fe}$  values ( $+0.177$  to  $+0.200\%$ ) for platy magnetite reveal a magmatic source, contrary to the low-T hydrothermal origin inferred from in situ trace element data. This inconsistency is proposed to be reconciled by considering the magmatic source associated with crystallized pyrrhotite, known for its lightest Fe isotope composition. Furthermore, the  $\delta^{18}\text{O}$  values of magnetite ( $+0.6$  to  $+4.6\%$ ) in the Beizhan deposit suggest that low-temperature hydrothermal fluids in the late stage may have modified the magnetite formed in the early stage.

**Author Contributions:** Conceptualization, Y.L. and D.W.; methodology, Y.L. and D.W.; software, Y.L.; validation, D.W.; formal analysis, Y.L. and D.W.; investigation, D.W. and Z.J.; resources, Z.Z. and Z.J.; data curation, D.W. and Y.L.; writing—original draft preparation, Y.L. and D.W.; writing—review and editing, Y.L., D.W. and Z.J.; visualization, Y.L.; supervision, D.W., Z.J., S.D. and Z.Z.; project administration, D.W. and Z.J.; funding acquisition, Z.J. and Z.Z. All authors have read and agreed to the published version of the manuscript.

**Funding:** This research was funded by the National Natural Science Foundation of China (grant 42172104), the National Scientific and Technological Supporting Key Project (2011BAB06B02) and the Project of China Geological Survey (DD20230040).

**Data Availability Statement:** All data are contained within this article.

**Acknowledgments:** We kindly thank Li Su for assistance with the LA ICP-MS analyses of magnetite and data reduction, and Zhenyu Chen for assistance with the EPMA analyses. The Third Geological Team of XBGMR is acknowledged for access to data and support with fieldwork. We are very grateful to the editor and reviewers for their thorough and constructive comments, which greatly improved the manuscript.

**Conflicts of Interest:** The authors declare no conflicts of interest.

## References

1. Zhang, Z.H.; Hong, W.; Jiang, Z.S.; Duan, S.G.; Li, F.M.; Shi, F.P. Geological characteristics and metallogenesis of iron deposits in western Tianshan, China. *Ore Geol. Rev.* **2014**, *57*, 425–440. [[CrossRef](#)]
2. Dong, L.H.; Feng, J.; Zhuang, D.Z.; Li, F.M.; Qu, X.; Liu, D.Q.; Tang, Y.L. Discussion of metallogenic models mineralization characteristics and main types of rich iron ores of Xinjiang. *Xinjiang Geol.* **2011**, *29*, 416–422. (In Chinese with English abstract).
3. Knipping, J.L.; Bilenker, L.D.; Simon, A.C.; Reich, M.; Barra, F.; Deditius, A.P.; Wälle, M.; Heinrich, C.A.; Holtz, F.; Munizaga, R. Trace elements in magnetite from massive iron oxide-apatite deposits indicate a combined formation by igneous and magmatic-hydrothermal processes. *Geochim. Et Cosmochim. Acta* **2015**, *171*, 15–38. [[CrossRef](#)]
4. Tornos, F.; Velasco, F.; Hanchar, J.M. Iron-rich melts, magmatic magnetite, and superheated hydrothermal systems: The El Laco deposit, Chile. *Geology* **2016**, *44*, 427–430. [[CrossRef](#)]
5. Xie, Q.H.; Zhang, Z.C.; Campos, E.A.; Deng, J.; Cheng, Z.G.; Fei, X.H.; Ke, S. Constraints of Fe-O isotopes on the origin of magnetite in the El Laco Kiruna-type iron deposit, Chile. *Ore Geol. Rev.* **2021**, *130*, 103967. [[CrossRef](#)]
6. Bilenker, L.D.; Simon, A.C.; Reich, M.; Lundstrom, C.C.; Gajos, N.; Bindeman, I.; Barra, F.; Munizaga, R. Fe-O stable isotope pairs elucidate a high-temperature origin of Chilean iron oxide-apatite deposits. *Geochim. Et Cosmochim. Acta* **2016**, *177*, 94–104. [[CrossRef](#)]
7. Nyström, J.O.; Billström, K.; Henríquez, F.; Fallick, A.E.; Naslund, H.R. Oxygen isotope composition of magnetite in iron ores of the Kiruna type in Chile and Sweden. *GFF* **2008**, *130*, 177–188. [[CrossRef](#)]
8. La Cruz, N.L.; Ovalle, J.T.; Simon, A.C.; Konecke, B.A.; Barra, F.; Reich, M.; Leisen, M.; Childress, T.M. The Geochemistry of Magnetite and Apatite from the El Laco Iron Oxide-Apatite Deposit, Chile: Implications for Ore Genesis. *Econ. Geol.* **2020**, *115*, 1461–1491. [[CrossRef](#)]

9. Day, W.C.; Slack, J.F.; Ayuso, R.A.; Seeger, C.M. Regional Geologic and Petrologic Framework for Iron Oxide  $\pm$  Apatite  $\pm$  Rare Earth Element and Iron Oxide Copper-Gold Deposits of the Mesoproterozoic St. Francois Mountains Terrane, Southeast Missouri, USA. *Econ. Geol.* **2016**, *111*, 1825–1858. [[CrossRef](#)]
10. Childress, T.M.; Simon, A.C.; Day, W.C.; Lundstrom, C.C.; Bindeman, I.N. Iron and Oxygen Isotope Signatures of the Pea Ridge and Pilot Knob Magnetite-Apatite Deposits, Southeast Missouri, USA. *Econ. Geol.* **2016**, *111*, 2033–2044. [[CrossRef](#)]
11. Johnson, C.A.; Day, W.C.; Rye, R.O. Oxygen, Hydrogen, Sulfur, and Carbon Isotopes in the Pea Ridge Magnetite-Apatite Deposit, Southeast Missouri, and Sulfur Isotope Comparisons to Other Iron Deposits in the Region. *Econ. Geol.* **2016**, *111*, 2017–2032. [[CrossRef](#)]
12. Günther, T.; Klemd, R.; Zhang, X.; Horn, I.; Weyer, S. In-situ trace element and Fe-isotope studies on magnetite of the volcanic-hosted Zhibo and Chagangnuoer iron ore deposits in the Western Tianshan, NW China. *Chem. Geol.* **2017**, *453*, 111–127. [[CrossRef](#)]
13. Zhang, Z.H.; Hong, W.; Jiang, Z.S.; Duan, S.G.; Xu, L.G.; Li, F.M.; Guo, X.C.; Zhao, Z.G. Geological Characteristics and Zircon U-Pb Dating of Volcanic Rocks from the Beizhan Iron Deposit in Western Tianshan Mountains, Xinjiang, NW China. *Acta Geol. Sin.-Engl. Ed.* **2012**, *86*, 737–747. [[CrossRef](#)]
14. Gao, J.; Long, L.L.; Klemd, R.; Qian, Q.; Liu, D.Y.; Xiong, X.M.; Su, W.; Liu, W.; Wang, Y.T.; Yang, F.Q. Tectonic evolution of the South Tianshan orogen and adjacent regions, NW China: Geochemical and age constraints of granitoid rocks. *Int. J. Earth Sci.* **2009**, *98*, 1221–1238. [[CrossRef](#)]
15. Jahn, B.-m.; Windley, B.; Natal'in, B.; Dobretsov, N. Phanerozoic continental growth in central Asia—Preface. *J. Asian Earth Sci.* **2004**, *23*, 599–603. [[CrossRef](#)]
16. Duan, S.G.; Zhang, Z.G.; Wang, D.C.; Jiang, Z.S.; Luo, W.J.; Li, F.M. Pyrite Re–Os and muscovite  $^{40}\text{Ar}/^{39}\text{Ar}$  dating of the Beizhan iron deposit in the Chinese Tianshan Orogen and its geological significance. *Int. Geol. Rev.* **2018**, *60*, 57–71. [[CrossRef](#)]
17. Yang, X.Q.; Liang, T.; Guo, X.C.; Zheng, Y.; Zhou, Y.; Chen, Z.H. Mineralogy and stable isotope constraints on the genesis of submarine volcanic-hosted Beizhan iron deposit in the Western Tianshan, NW China. *Geol. J.* **2018**, *53*, 329–344. [[CrossRef](#)]
18. Pan, H.D.; Shen, P.; Li, C.H.; Feng, H.X.; Wu, Y.; Guo, X.C.; Zhang, J.S. Discovery and Geological Significance of Siliceous Rocks in Beizhan Iron Deposit. *J. Earth Sci. Environ.* **2021**, *43*, 785–799. [[CrossRef](#)]
19. Li, H.; Zhang, Z.; Liu, B.; Jin, Y.; Santosh, M. The genetic link between iron oxide-apatite and iron skarn mineralization in the Beizhan deposit, Western Tianshan, NW China: Evidence from magnetite and gangue mineral geochemistry. *J. Asian Earth Sci.* **2023**, *241*, 1367–9120. [[CrossRef](#)]
20. Canil, D.; Lacourse, T. Geothermometry using minor and trace elements in igneous and hydrothermal magnetite. *Chem. Geol.* **2020**, *541*, 119576. [[CrossRef](#)]
21. Gao, J.; Li, M.S.; Xiao, X.C.; Tang, Y.Q.; He, G.Q. Paleozoic tectonic evolution of the Tianshan Orogen, northwestern China. *Tectonophysics* **1998**, *287*, 213–231, (In Chinese with English abstract). [[CrossRef](#)]
22. Klemd, R.; Gao, J.; Li, J.L. Metamorphic evolution of (ultra)-high-pressure subduction-related transient crust in the South Tianshan Orogen (Central Asian Orogenic Belt): Geodynamic implications. *Gondwana Res.* **2015**, *28*, 1–25. [[CrossRef](#)]
23. Qian, Q.; Gao, J.; Klemd, R.; He, G.Q.; Song, B.A.; Liu, D.Y.; Xu, R.H. Early Paleozoic tectonic evolution of the Chinese South Tianshan Orogen: Constraints from SHRIMP zircon U-Pb geochronology and geochemistry of basaltic and dioritic rocks from Xiata, NW China. *Int. J. Earth Sci.* **2009**, *98*, 551–569. [[CrossRef](#)]
24. Gao, J.; Qian, Q.; Long, L.L.; Zhang, X.; Li, J.L.; Su, W. Accretionary orogenic process of western Tianshan, China. *Geol. Bull. China* **2009**, *28*, 1804–1816, (In Chinese with English abstract).
25. Li, J.L.; Su, W.; Zhang, X.; Liu, X. Zircon Cameca U-Pb dating and its significance for granulite-facies gneisses from the western Awulale Mountain, West Tianshan, China. *Geol. Bull. China* **2009**, *28*, 1852–1862, (In Chinese with English abstract).
26. Hu, A.Q.; Wei, G.J.; Jiang, B.M.; Zhang, J.B.; Deng, W.F.; Chen, L.L. Formation of the 0.9 Ga Neoproterozoic granitoids in the Tianshan Orogen, NW China: Constraints from the SHRIMP zircon age determination and its tectonic significance. *Geochimica* **2010**, *39*, 197–212. [[CrossRef](#)]
27. Kroner, A.; Kovach, V.; Belousova, E.; Hegner, E.; Armstrong, R.; Dolgoplova, A.; Seltmann, R.; Alexeiev, D.V.; Hoffmann, J.E.; Wong, J. Reassessment of continental growth during the accretionary history of the Central Asian Orogenic Belt. *Gondwana Res.* **2014**, *25*, 103–125. [[CrossRef](#)]
28. Windley, B.F.; Alexeiev, D.; Xiao, W.J.; Kroner, A.; Badarch, G. Tectonic models for accretion of the Central Asian Orogenic Belt. *J. Geol. Soc.* **2007**, *164*, 31–47. [[CrossRef](#)]
29. Yang, F.Q.; Mao, J.W.; Bierlein, F.P.; Pirajno, F.; Zhao, C.S.; Ye, H.S.; Liu, F. A review of the geological characteristics and geodynamic mechanisms of Late Paleozoic epithermal gold deposits in North Xinjiang, China. *Ore Geol. Rev.* **2009**, *35*, 217–234. [[CrossRef](#)]
30. Zhang, Z.H.; Hong, W.; Jiang, Z.S.; Duan, S.G.; Wang, Z.H.; Li, F.M.; Shi, F.P.; Zhao, J.; Zheng, R.Q. Geological features, mineralization types and metallogenic setting of Late Paleozoic iron deposits in western Tianshan Mountains of Xinjiang. *Miner. Depos.* **2012**, *31*, 941–964. [[CrossRef](#)]
31. Zhang, Z.C.; Li, H.M.; Li, J.W.; Song, X.Y.; Hu, H.; Li, L.X.; Chai, F.M.; Hou, T.; Xu, D.R. Geological settings and metallogenesis of high-grade iron deposits in China. *Sci. China Earth Sci.* **2021**, *64*, 691–715. [[CrossRef](#)]
32. Duan, S.G.; Zhang, Z.H.; Jiang, Z.S.; Zhao, J.; Zhang, Y.P.; Li, F.M.; Tian, J.Q. Geology, geochemistry, and geochronology of the Dundee iron–zinc ore deposit in western Tianshan, China. *Ore Geol. Rev.* **2014**, *57*, 441–461. [[CrossRef](#)]

33. Hong, W.; Zhang, Z.H.; Li, F.M.; Liu, X.Z. Stable isotopic characteristics of the Chagangnuoer iron deposit in Western Tianshan, Xinjiang and its geological significance. *Rock Miner. Anal.* **2012**, *31*, 1077–1087. [[CrossRef](#)]
34. Jiang, Z.S.; Zhang, Z.H.; Wang, Z.H.; Duan, S.G.; Li, F.M.; Tian, J.Q. Geology, geochemistry, and geochronology of the Zhibo iron deposit in the Western Tianshan, NW China Constraints on metallogenesis and tectonic setting. *Ore Geol. Rev.* **2014**, *57*, 406–424. [[CrossRef](#)]
35. Wang, C.L.; Wang, Y.T.; Dong, L.H.; Qin, K.Z.; Evans, N.J.; Zhang, B.; Ren, Y. Iron mineralization at the Songhu deposit, Chinese Western Tianshan: A type locality with regional metallogenic implications. *Int. J. Earth Sci.* **2018**, *107*, 291–319. [[CrossRef](#)]
36. Zhang, X.; Klemd, R.; Gao, J.; Dong, L.H.; Wang, X.S.; Haase, K.; Jiang, T.; Qian, Q. Metallogenesis of the Zhibo and Chagangnuoer volcanic iron oxide deposits in the Awulale Iron Metallogenic Belt, Western Tianshan orogen, China. *J. Asian Earth Sci.* **2015**, *113*, 151–172. [[CrossRef](#)]
37. Shan, Q.; Zhang, B.; Luo, Y.; Zhou, C.B.; Yu, X.Y.; Zeng, Q.S.; Yang, W.B.; Niu, H.C. Characteristics and trace element geochemistry of pyrite from the Songhu iron deposit, Nilek County, Xinjiang, China. *Acta Petrol. Sin.* **2009**, *25*, 1456–1464, (In Chinese with English abstract).
38. Wang, B.Y.; Hu, X.J.; Wang, J.T.; Shao, Q.H.; Ling, J.L.; Guo, N.X.; Zhao, Y.F.; Xia, Z.D.; Jiang, C.Y. Geological characteristics and genesis of Chagannur iron deposit in Western Tianshan, Xinjiang. *Miner. Depos.* **2011**, *30*, 385–402. [[CrossRef](#)]
39. Chen, Y.C.; Liu, D.Q.; Tang, Y.L.; Wang, D.H.; Dong, L.H.; Xu, X.; Wang, X.D. *Mineral Resources and Mineralization System in Tianshan, China*; Geological Publishing House: Beijing, China, 2008; Volume 1, pp. 246–287, (In Chinese with English abstract).
40. Duan, S.G.; Zhang, Z.H.; Wang, D.C.; Li, F.M. Geology, Geochemistry and Zircon U-Pb Geochronology of Porphyries in the Dabate Mo-Cu Deposit, Western Tianshan, China: Petrogenesis and Tectonic Implications. *Acta Geol. Sin.-Engl. Ed.* **2017**, *91*, 530–544. [[CrossRef](#)]
41. Jiang, Z.S.; Wang, D.C.; Zhang, Z.H.; Duan, S.G.; Kang, Y.J.; Li, F.M. Application of in situ titanite U-Pb geochronology to volcanic-hosted magnetite deposit: New constraints on the timing and genesis of the Zhibo deposit, Western Tianshan, NW China. *Ore Geol. Rev.* **2018**, *95*, 325–341. [[CrossRef](#)]
42. Ge, S.S.; Zhai, M.G.; Safonova, I.; Li, D.P.; Zhu, X.Y.; Zuo, P.F.; Shan, H.X. Whole-rock geochemistry and Sr-Nd-Pb isotope systematics of the Late Carboniferous volcanic rocks of the Awulale metallogenic belt in the western Tianshan Mountains (NW China): Petrogenesis and geodynamical implications. *Lithos* **2015**, *228*, 62–77. [[CrossRef](#)]
43. Han, C.M.; Xiao, W.J.; Su, B.X.; Sakyi, P.A.; Ao, S.J.; Zhang, J.; Wan, B.; Song, D.F.; Zhang, Z.Y.; Wang, Z.M. Late Paleozoic metallogenesis and evolution of the Chinese Western Tianshan Collage, NW China, Central Asia orogenic belt. *Ore Geol. Rev.* **2020**, *124*, 103643. [[CrossRef](#)]
44. Feng, W.Y.; Zhu, Y.F. Petrogenesis and tectonic implications of the late Carboniferous calc-alkaline and shoshonitic magmatic rocks in the Awulale mountain, western Tianshan. *Gondwana Res.* **2019**, *76*, 44–61. [[CrossRef](#)]
45. Sun, L.H.; Wang, Y.J.; Fan, W.M.; Zi, J.W. Post-collisional potassic magmatism in the Southern Awulale Mountain, western Tianshan Orogen: Petrogenetic and tectonic implications. *Gondwana Res.* **2008**, *14*, 383–394. [[CrossRef](#)]
46. Shen, P.; Pan, H.D.; Li, C.H.; Feng, H.X.; Wu, Y.; Shi, F.P.; Guo, X.C.; Li, W.G. Carboniferous ore-controlling volcanic apparatus and metallogenic models for the large-scale iron deposits in the Western Tianshan, Xinjiang. *Acta Petrol. Sin.* **2020**, *36*, 2845–2868. [[CrossRef](#)]
47. Luo, W.J.; Zhang, Z.H.; Duan, S.G.; Jiang, Z.S.; Wang, D.C.; Chen, J. Mineral geochemistry of Beizhan mafic-ultramafic rocks, West Tianshan Mountains, Xinjiang: Constraints on genesis of Beizhan iron deposit. *Miner. Depos.* **2020**, *39*, 419–437, (In Chinese with English abstract).
48. Zhang, X.; Tian, J.Q.; Gao, J.; Klemd, R.; Dong, L.H.; Fan, J.J.; Jiang, T.; Hu, C.J.; Qian, Q. Geochronology and geochemistry of granitoid rocks from the Zhibo syngenetic volcanogenic iron ore deposit in the Western Tianshan Mountains (NW-China): Constraints on the age of mineralization and tectonic setting. *Gondwana Res.* **2012**, *22*, 585–596. [[CrossRef](#)]
49. Han, Q.; Gong, X.P.; Cheng, S.L.; Zhang, J.; Song, X.L.; Feng, J.; Pan, Z.C.; Xie, L.; Su, H.; Liu, X.L. Zircon U-Pb geochronology and Hf isotopes of volcanic rocks in Beizhan iron ore of the west Tianshan. *Acta Geol. Sin.* **2015**, *89*, 70–82. [[CrossRef](#)]
50. Sun, J.M.; Ma, Z.P.; Xu, X.Y.; Li, X.Y.; Weng, K.; Zhang, T. The formation epoch of the host wall rock of the Beizhan iron deposit in West Tianshan Mountains of Xinjiang and its geological significance. *Geol. Bull. China* **2012**, *31*, 1973–1982, (In Chinese with English abstract).
51. Duan, S.G.; Jiang, Z.S.; Luo, W.J. Geochronology and Geochemistry of Volcanic and Intrusive Rocks from the Beizhan Iron Deposit, Western Xinjiang, NW China: Petrogenesis and Tectonic Implications. *Minerals* **2024**, *14*, 16. [[CrossRef](#)]
52. Huang, F.; Zhang, Z.F.; Lundstrom, C.C.; Zhi, X.C. Iron and magnesium isotopic compositions of peridotite xenoliths from Eastern China. *Geochim. Et Cosmochim. Acta* **2011**, *75*, 3318–3334. [[CrossRef](#)]
53. Clayton, R.N.; Mayeda, T.K. The use of bromine pentafluoride in the extraction of oxygen from oxides and silicates for isotope analysis. *Geochim. Et Cosmochim. Acta* **1963**, *27*, 43–52. [[CrossRef](#)]
54. Rudnick, R.L.; Gao, S.; Holland, H.D.; Turekian, K.K. Composition of the continental crust. *Treatise Geochem.* **2003**, *3*, 1–64.
55. Dare, S.A.S.; Barnes, S.J.; Beaudoin, G. Variation in trace element content of magnetite crystallized from a fractionating sulfide liquid, Sudbury, Canada: Implications for provenance discrimination. *Geochim. Et Cosmochim. Acta* **2012**, *88*, 27–50. [[CrossRef](#)]
56. Wang, T. Geological Characteristics and Ore Genesis of Beizhan Iron Mine, Western Tianshan, Xinjiang. Master's Dissertation, China University of Geosciences, Beijing, China, 2014; pp. 1–95, (In Chinese with English abstract).

57. Luo, W.J.; Sun, J. Oxygen isotope geochemistry of Fe oxide minerals and its applications to the study of iron ore deposit. *Acta Petrol. Et Mineral.* **2019**, *38*, 121–130. (In Chinese with English abstract).
58. Li, D.P. Superimposition, Mineralization of the Awulale Iron Deposit Belt in Western Tishan, Xinjiang. Ph.D. Dissertation, China University of Geosciences, Beijing, China, 2012; pp. 1–147. (In Chinese with English abstract).
59. Jiang, Z.S. Carboniferous Volcanism and Fe Mineralization at the Zhibo Iron Deposit in the Western Tianshan. Ph.D. Dissertation, Chinese Academy of Geological Sciences, Beijing, China, 2014; pp. 1–179. (In Chinese with English abstract).
60. Dupuis, C.; Beaudoin, G. Discriminant diagrams for iron oxide trace element fingerprinting of mineral deposit types. *Miner. Depos.* **2011**, *46*, 319–335. [[CrossRef](#)]
61. Maia, M.; Barrulas, P.; Nogueira, P.; Mirao, J.E.; Noronha, F. In situ LA-ICP-MS trace element analysis of magnetite as a vector towards mineral exploration: A comparative case study of Fe-skarn deposits from SW Iberia (Ossa-Morena Zone). *J. Geochem. Explor.* **2022**, *234*, 106941. [[CrossRef](#)]
62. Nadoll, P.; Mauk, J.L.; Leveille, R.A.; Koenig, A.E. Geochemistry of magnetite from porphyry Cu and skarn deposits in the southwestern United States. *Miner. Depos.* **2015**, *50*, 493–515. [[CrossRef](#)]
63. Deditius, A.P.; Reich, M.; Simon, A.C.; Suvorova, A.; Knipping, J.; Roberts, M.P.; Rubanov, S.; Dodd, A.; Saunders, M. Nanogeochemistry of hydrothermal magnetite. *Contrib. Mineral. Petrol.* **2018**, *173*, 1. [[CrossRef](#)]
64. Nadoll, P.; Angerer, T.; Mauk, J.L.; French, D.; Walshe, J. The chemistry of hydrothermal magnetite: A review. *Ore Geol. Rev.* **2014**, *61*, 1–32. [[CrossRef](#)]
65. Dare, S.A.S.; Barnes, S.J.; Beaudoin, G.; Méric, J.; Boutroy, E.; Potvin-Doucet, C. Trace elements in magnetite as petrogenetic indicators. *Miner. Depos.* **2014**, *49*, 785–796. [[CrossRef](#)]
66. Nadoll, P.; Mauk, J.L.; Hayes, T.S.; Koenig, A.E.; Box, S.E. Geochemistry of magnetite from hydrothermal ore deposits and host rocks of the Mesoproterozoic Belt Supergroup, United States. *Econ. Geol.* **2012**, *107*, 1275–1292. [[CrossRef](#)]
67. Duan, C.; Li, Y.h.; Mao, J.W.; Hou, K.J.; Wang, C.L.; Yang, B.Y.; Wang, Q.; Li, W. Ore formation at the Washan iron oxide–apatite deposit in the Ningwu Ore District, eastern China: Insights from in situ LA-ICP-MS magnetite trace element geochemistry. *Ore Geol. Rev.* **2019**, *112*, 103064. [[CrossRef](#)]
68. Taylor, H.P., Jr. The oxygen isotope geochemistry of igneous rocks. *Contrib. Mineral. Petrol.* **1968**, *19*, 1–71. [[CrossRef](#)]
69. Palma, G.; Reich, M.; Barra, F.; Ovalle, J.T.; Real, I.D.; Simon, A.C. Thermal evolution of Andean iron oxide–apatite (IOA) deposits as revealed by magnetite thermometry. *Sci. Rep.* **2021**, *11*, 18424. [[CrossRef](#)] [[PubMed](#)]
70. Troll, V.R.; Weis, F.A.; Jonsson, E.; Andersson, U.B.; Majidi, S.A.; Högdahl, K.; Harris, C.; Millet, M.-A.; Chinnasamy, S.S.; Kooijman, E.; et al. Global Fe–O isotope correlation reveals magmatic origin of Kiruna-type apatite–iron–oxide ores. *Nat. Commun.* **2019**, *10*, 1712. [[CrossRef](#)]
71. Beard, B.L.; Johnson, C.M.; Von Damm, K.L.; Poulson, R.L. Iron isotope constraints on Fe cycling and mass balance in oxygenated Earth oceans. *Geology* **2003**, *31*, 629–632. [[CrossRef](#)]
72. Beard, B.L.; Johnson, C.M. Inter-mineral Fe isotope variations in mantle-derived rocks and implications for the Fe geochemical cycle. *Geochim. Et Cosmochim. Acta* **2004**, *68*, 4727–4743. [[CrossRef](#)]
73. Craddock, P.R.; Warren, J.M.; Dauphas, N. Abyssal peridotites reveal the near-chondritic Fe isotopic composition of the Earth. *Earth Planet. Sci. Lett.* **2013**, *365*, 63–76. [[CrossRef](#)]
74. Telus, M.; Dauphas, N.; Moynier, F.; Tissot, F.L.H.; Teng, F.-Z.; Nabelek, P.I.; Craddock, P.R.; Groat, L.A. Iron, zinc, magnesium and uranium isotopic fractionation during continental crust differentiation: The tale from migmatites, granitoids, and pegmatites. *Geochim. Et Cosmochim. Acta* **2012**, *97*, 247–265. [[CrossRef](#)]
75. Dauphas, N.; Craddock, P.R.; Asimow, P.D.; Bennett, V.C.; Nutman, A.P.; Ohnenstetter, D. Iron isotopes may reveal the redox conditions of mantle melting from Archean to Present. *Earth Planet. Sci. Lett.* **2009**, *288*, 255–267. [[CrossRef](#)]
76. Williams, H.M.; Nielsen, S.G.; Renac, C.; Griffin, W.L.; O'Reilly, S.Y.; McCammon, C.A.; Pearson, N.; Viljoen, F.; Alt, J.C.; Halliday, A.N.J.E.; et al. Fractionation of oxygen and iron isotopes by partial melting processes: Implications for the interpretation of stable isotope signatures in mafic rocks. *Earth Planet. Sci. Lett.* **2009**, *283*, 156–166. [[CrossRef](#)]
77. Weis, F. Oxygen and Iron Isotope Systematics of the Grängesberg Mining District (GMD). Ph.D. Dissertation, Uppsala Universitet, Uppsala, Sweden, 2013; pp. 1–77.
78. Wang, Y.; Zhu, X.K.; Mao, J.W. Iron isotope fractionation during skarn-type metallogeny: A case study of Xinqiao Cu–S–Fe–Au deposit in the Middle-Lower Yangtze valley. *Ore Geol. Rev.* **2011**, *43*, 194–202. [[CrossRef](#)]
79. Zhou, Z.J.; Tang, H.S.; Chen, Y.J.; Chen, Z.L. Trace elements of magnetite and iron isotopes of the Zankan iron deposit, westernmost Kunlun, China: A case study of seafloor hydrothermal iron deposits. *Ore Geol. Rev.* **2016**, *80*, 1191–1205. [[CrossRef](#)]
80. Zheng, J.H.; Chen, B.; Liu, S.J.; Bao, C. Iron isotope fractionation in reduced hydrothermal gold deposits: A case study of the Wulong gold deposit, Liaodong Peninsula, East China. *Am. Mineral.* **2021**, *106*, 430–442. [[CrossRef](#)]
81. Xue, S.; Niu, Y.L.; Chen, Y.H.; Shi, Y.N.; Xia, B.Y.; Wang, P.Y.; Gong, H.M.; Wang, X.H.; Duan, M. Iron Isotope Fractionation during Skarn Cu–Fe Mineralization. *Minerals* **2021**, *11*, 444. [[CrossRef](#)]
82. Hu, H.; Li, J.W.; Lentz, D.; Ren, Z.; Zhao, X.F.; Deng, X.D.; Hall, D. Dissolution–reprecipitation process of magnetite from the Chengchao iron deposit: Insights into ore genesis and implication for in-situ chemical analysis of magnetite. *Ore Geol. Rev.* **2014**, *57*, 393–405. [[CrossRef](#)]
83. Taylor, H.P.J.R. Oxygen isotope studies of hydrothermal mineral deposits. In *Geochemistry of Hydrothermal Ore Deposits*; Bames, H.L., Ed.; John Wiley & Sons: New York, NY, USA, 1967; pp. 109–142.

84. Heimann, A.; Beard, B.L.; Johnson, C.M. The role of volatile exsolution and sub-solidus fluid/rock interactions in producing high  $^{56}\text{Fe}/^{54}\text{Fe}$  ratios in siliceous igneous rocks. *Geochim. Et Cosmochim. Acta* **2008**, *72*, 4379–4396. [[CrossRef](#)]
85. Hou, L.; Guo, L.N.; Xu, S.W.; Zhang, Q.M.; Ting, Z.X. In situ geochemistry and Fe–O isotopic composition of iron oxides from the Pha Lek Fe deposit, northwest Truong Son orogenic belt, Laos: Implications for ore-forming processes. *Miner. Depos.* **2021**, *56*, 1405–1421. [[CrossRef](#)]
86. Zheng, J.H.; Mao, J.W.; Yang, F.Q.; Chai, F.M.; Zhu, Y.F. Mineralogy, fluid inclusions, and isotopes of the Cihai iron deposit, eastern Tianshan, NW China: Implication for hydrothermal evolution and genesis of subvolcanic rocks-hosted skarn-type deposits. *Ore Geol. Rev.* **2017**, *86*, 404–425. [[CrossRef](#)]
87. Jonsson, E.; Troll, V.R.; Högdahl, K.; Harris, C.; Weis, F.; Nilsson, K.P.; Skelton, A. Magmatic origin of giant ‘Kiruna-type’ apatite-iron-oxide ores in Central Sweden. *Sci. Rep.* **2013**, *3*, 1644. [[CrossRef](#)] [[PubMed](#)]

**Disclaimer/Publisher’s Note:** The statements, opinions and data contained in all publications are solely those of the individual author(s) and contributor(s) and not of MDPI and/or the editor(s). MDPI and/or the editor(s) disclaim responsibility for any injury to people or property resulting from any ideas, methods, instructions or products referred to in the content.